Powell Lens-based Line-Scan Spectral Domain Optical Coherence Tomography for Cellular Resolution Imaging of Biological Tissues

by

Weixiang Song

A thesis

presented to the University of Waterloo

in fulfillment of the

thesis requirement for the degree of

Master of Science

in

Physics

Waterloo, Ontario, Canada, 2022

Author’s Declaration

I hereby declare that I am the sole author of this thesis. This is a true copy of the thesis, including any required final revisions, as accepted by my examiners.

I understand that my thesis may be made electronically available to the public.

Abstract

The cornea is the transparent and dome-shaped front part of the eye that covers the anterior chamber of the eye. As the primary interface between the surrounding environment and other intraocular organs, its health is critical for clear vision. Both ocular diseases specific to the cornea such as keratoconus and Fuchs' dystrophy, as well as systemic diseases such as diabetes can cause morphological and physiological changes in the cornea. At the early stages of disease development when treatment could be most beneficial, these changes occur on cellular level. The ability to visualize these microscale changes can allow for early diagnostics and timely medical interventions for various ophthalmic diseases. This necessitates development of optical imaging technologies that can provide all of the following requirements: a) non-invasive (non-contact) examination of the corneal tissue; imaging resolution in the order of few micrometers, to allow for visualization of cellular and sub-cellular structures; c) rapid, volumetric image acquisition, to allow for eye-motion artefacts free images.

Optical coherence tomography (OCT) is a non-invasive imaging technology that has captured the growing interest of clinicians and scientists. It stands outs from other conventional ophthalmic imaging tools as it combines micrometer-scale resolution, very high sensitivity, and ultrahigh image acquisition speed. Traditionally, OCT uses a point scanning design where the focused imaging beam (circular beam with Gaussian intensity profile) is raster-scanned in the XY plane to acquire a volumetric image of the imaged object. Due to technology limitations, the B-scan rate of point-scanning OCT systems can rarely exceed 1,000 B-scans/sec without severe restrictions on the imaged field-of-view (FOV) and the number of acquired A-scans and B-scans. The slower scanning rate results in increased susceptibility of the OCT images to eye-motion induced image artifacts. Line-scan (LS) OCT offers a new optical design where the imaging beam is projected onto the imaged object in the form of a very thin line that is scanned only in Y direction in order to generate volumetric OCT images. Due to the reduced mechanical scanning, LS-OCT systems can reach image acquisition tares of 20,000 B-scans/s or higher, therefore eliminating majority of the eye-motion induced image artefacts. Traditionally, LS-OCT utilizes cylindrical lenses to generate the line beam, however the intensity distribution of the line is not uniform, and the line has elliptical instead of rectangular shape. This causes spatially dependent variation of the LS-OCT system’s SNR over the FOV. The main goal of this research project was to develop a high-speed LS spectral domain OCT (LS-SD-OCT) system for cellular resolution imaging of biological tissues, including the human cornea, with improved uniformity of the SNR over the FOV.

An LS-SD-OCT system that uses a Powell lens instead of a cylindrical lens to generate the line beam profile, was designed and built (PL-LS-SD-OCT). The Powell lens allowed for generation of a rectangular beam profile (compared to elliptical one generated by cylindrical lenses) with almost uniform intensity distribution over the beam profile. By utilizing a broadband light source and high-speed area camera, the PL-LS-SD-OCT system is able to achieve lateral resolutions of ~2μm and ~4μm in the X and Y directions respectively, axial resolution of ~1.9μm and maximum frame rate of 1000 B-scans/sec for 550 illuminated pixels in spectral direction. The performance of the new PL-LS-SD-OCT system was tested by imaging ex-vivo different biological tissues such as cucumber and mouse cornea. Individual cells and cellular nuclei are visible in the cucumber images. The mouse cornea images allowed clear identification of the major corneal layers such as the epithelium, stroma and endothelium.

Further optimization of the system's design is necessary to adapt the system for human ophthalmic imaging. The proposed PL-LS-SD-OCT system could be used for numerous biomedical applications in ophthalmology, dermatology, etc.

Acknowledgements

I greatly thank Prof. Bizheva for her guidance and help with the research and many other aspects of my life. She taught me how OCT works, from the fundamentals to the advancements, and helped me grow as a researcher. She has always been patient and understanding whenever I faced challenges in the lab or encountered troubles in my life. It was a great pleasure to work with you.

I would also like to thank Han Le, who was a senior student during my study. He offered me tremendous help in programming and lab equipment training. Han, I couldn't even imagine what an unpromising situation I would be sitting in without your support. I am so happy that you successfully graduated, and I wish you all the best in the next chapter of your life.

A special thanks to my dear friends Hadiya Ma and Sandra Cheng. You cannot imagine how lucky I feel to have you guys in my life. It is so unbelievable that we have spent so many years together from Queen's to UW. Though now we are sailing apart to different places in the world, I wish you the brightest future and the happiest life no matter where you are.

Table of Contents

List of Figures

List of Tables

Chapter 1 Introduction

1.1 Motivation

Following cataracts, corneal diseases are the world's second most significant cause of blindness [1,2]. For example, trachoma causes scarring and vascularization of the cornea and is responsible for blinding 4.9 million individuals. Ocular trauma and corneal ulceration also cause 1.5-2.0 million new blindness cases yearly [1]. The cornea is a thin layer of transparent tissue that comprises the outermost part of the eye. It serves as a frontier barrier that protects the inner ocular structure and provides approximately two-thirds of the total refractive power of the eye [3]. Thus, proper functioning of the cornea is key to clear vision. Though the cornea has some regenerative mechanisms, trauma ocular pathologies and systemic diseases can all cause acute or irreversible damage to the corneal tissue that may result in severe visual impairment [3,4].

Traditional ophthalmic assessment methods such as slit lamp examination and ultrasound biomicroscope help provide in-vivo assessment of ocular tissues. They have been widely used in clinics for their low cost and ease of use [5]. However, the resolution obtained with these methods is insufficient to image pathological tissue on a cellular lever, making it only able to examine the disease after its maturity, which is often too late for effective treatment. A major advancement in ophthalmic imaging resolutions has been made with the development of in-vivo confocal microscopy (IVCM) [6]. Commercially available IVCM technology can achieve lateral resolution of several microns. Such high resolution enables cellular level enface imaging that can help diagnose morphological changes in the early stages of ophthalmic diseases and allow timely medical interventions [6]. Nevertheless, IVCM has some significant limitations: acquisition of volumetric images is relatively slow as it requires mechanical axial scanning, therefore volumetric IVCM images are susceptible to eye motion artefacts; the FOV is typically restricted to a few hundred microns, and the axial resolution is not high enough to allow for imaging individual cells in the axial direction [7,8].

Optical coherence tomography (OCT) is an optical imaging modality based on low coherence interferometry, that can acquire high-resolution volumetric images of biological tissue in-vivo and non-invasively [9]. The early OCT technology was based on a time-domain (TD-OCT) design that required mechanical scanning of the reference mirror and therefor limited the image acquisition rate to < 1 B-scan/sec. This slow mechanical scanning resulted in significant distortions of ophthalmic cross-sectional OCT images and prevented acquisition of volumetric OCT images due to involuntary eye motion [9]. Some of the slow scanning issues were solved at the beginning of the 21st century with the

development of Fourier-domain (FD) OCT, which offers 2 major optical designs: spectral domain OCT (SD-OCT) that utilizes as continuous wavelength light source and spectrometer + line-scan camera at the detection end; and swept source OCT (SS-OCT), that utilizes a tunable light source and a dual-balanced photodetector unit at the detection end of the system[9,10,11]. The image acquisition rate of FD-OCT is limited by the acquisition rate of the linear array camera (SD-OCT) and the sweep rate of the tunable laser (SS-OCT) and currently can reach ~1,000 B-scans/sec or higher. However, volumetric FD-OCT ophthalmic images are still susceptible to high frequency ocular motion especially at micrometer scale resolution [9]. Over the past 10 years, the OCT image acquisition rate has been improved by developing line-field or the line-scan (LS) OCT which uses only 1D mechanical scanning and can reach image acquisition rates as high as 20,000 B-scans/sec [12,13].

1.2 Thesis objectives

The main goal of the research presented in this thesis was to develop LS-OCT technology with: a) improved uniform sensitivity over the entire FOV by utilizing a Powell lens (an aspheric lens that expands the incident collimated beam into a line with a specific fan angle) to generate a rectangularly shaped imaging beam with almost uniform intensity profile; b) improved axial resolution, by employing a broadband light source; c) larger scanning range, by utilizing a camera with larger number of pixels in the spectral direction; d) high imaging rate > 4,000 B-scans/sec while preserving the high axial resolution, large FOV and extended scanning range.

1.3 Organization of the thesis

The contents of this thesis are organized as follows:

- Chapter 2 presents an overview of the corneal anatomy and of imaging modalities used for clinical assessment of the corneal morphology.
- Chapter 3 reviews in-depth the principles of operation of OCT and its major characteristics such as spatial resolution, scanning range, SNR, etc.
- Chapter 4 discusses the optical design of the PL-LS-OCT system.
- Chapter 5 reviews results from the system characterization and testing.
- Chapter 6 offer a discussion of the current results and plans for future work.

Chapter 2 Background

2.1 Corneal anatomy

The transparent cornea and the thin transparent layer of tissue over the white-colored opaque sclera called conjunctiva constitute the eye's outermost layer, serving as a protective barrier to keep the inside structure of the eye from physical damage and infections [3]. In healthy adults, the cornea is oval-shaped with an average vertical diameter in the range of 9 mm – 11 mm and is about 1 mm elongated in the horizontal direction [3]. The average thickness of the cornea in healthy adults is about 550 μm in the center, increasing gradually to about 630 μm towards the peripheral area. These measurements can have ± 100 μm fluctuations depending on age, gender, and the extension directions (superior, inferior, temporal, and nasal) [4]. The normal, healthy cornea's curvature is steeper centrally and flattens as it extends outward. With a refractive index of 1.376, it forms a convex and aspherical optical system that provides approximately 70% of the total refractive power of the eye [3]. It is comprised of five major layers, listed here from outside to inside: the epithelium, the Bowman's layer, the stroma, the Descemet's membrane, and the endothelium [4,14]. Corneal diseases or dystrophies such as keratoconus can cause significant thinning and thickening of the total corneal and its individual layers, as well as change significantly the corneal curvature that can result in significant visual changes such as blur and double vision [14,15].

2.1.1 Epithelium

The epithelial layer consists of 4 to 6 layers of cells that can be classified in three types: superficial cells, wing cells, and basal cells. Together, they build up a total epithelial thickness of about 40 μm to 50 μm. The epithelial surface is in contact with a tear film, which lubricates the eyeball, smoothens out the micro irregularities for clear vision, and provides a primary defense line against foreign material [3,4,6]. The epithelial cells are tightly packed to prevent the inside structure from the outer environment, though they allow nutrients and oxygen from the tear film to pass through. In addition, the epithelium has a unique self-regeneration property among all corneal layers, maintained by the stem cells in the limbus. With a 7 to 10 days cycle, epithelial cells undergo involution, apoptosis, and desquamation as deeper cells replace dying superficial cells [16].

Being the outermost part of the eye, the epithelium bears the highest risk of being physically damaged as. Malfunctioning of the epithelium can immediately affect vision and make the rest part of

the cornea more vulnerable [17,18]. Usually, minor epithelial defects can heal rapidly, thanks to their self-renewable ability. However, more severe damage can occur due to many risk factors such as mechanical trauma, diabetic keratopathy, exposure keratopathy, ultraviolet burns, decreased tear production, limbal stem cell deficiency, neurotrophic keratopathy, and infection, which can delay or halt the healing process [16].

2.1.2 Bowman's layer

The bowman's layer is a smooth yet tough acellular interface between epithelium and stroma, about 12 to 15 μm in thickness. It is the condensate of the most anterior part of the stroma that helps support the corneal geometry. This layer is not regenerative and will leave scars when damaged [3,4]. Though it has no critical corneal physiological function, it can be used as a visible indicator for investigating stromal-epithelial interactions [19].

Bowman's layer defects are often related to the epithelium. Common causes include mechanical trauma above the epithelium resulting in scars, and corneal dystrophy, which is a genetic disease that causes cloudiness [20].

2.1.3 Stroma

The stroma is the thickest layered structure in the cornea, which consists of a meshwork of collagen fibers with keratocyte cells embedded among the fibers, taking up about 80% to 85% of the total corneal thickness. Fibrils are formed from collagen fibers arranged in parallel bundles, and a pack of horizontally arranged fibrils comprises a fabric sheet called lamellae. A healthy adult cornea can contain 200 to 250 layers of distinct lamellae [3,4]. Lamellae are firmly appressed together with a perpendicular orientation between the adjacent neighbors. This particular arrangement is critical for stromal transparency and differs the stroma from other collagenous structures in the body [21,22]. Lamellae in the anterior stroma have greater packing density. In addition, they are highly interwoven and rigid, which is responsible for providing the strength for the cornea to maintain its shape. At the same time, the posterior lamellae are less interlaced and can swell through hydration from the endothelial layer. However, they appear more organized than the superficial layers [3,4,22]. This latticed network of collagen fibers is also known as the extracellular matrix (ECM). Keratocytes are the primary type of cells in the stroma. They are interconnected and sparsely distributed among the spacings between lamellae. Keratocytes can produce collagen molecules and glycosaminoglycans,

which act like glue to build fibers into complex structures. Thus, keratocytes are in charge of the ECM environment maintenance, including repairing damaged fibers and maintaining stromal homeostasis [3,4].

Upon injuries, the stroma can heal by triggering the repairing mechanism of keratocytes. Like the wound healing process in skins, stroma recovery undergoes three stages: repair, regeneration, and remodeling [23]. The most common stromal diseases are corneal stromal dystrophies, which belong to a sub-category in corneal dystrophies. Such dystrophies involve a group of non-inflammatory, inherited, bilateral disorders, which can cause pathognomonic patterns of corneal deposition and morphological changes. There are three main types of phenotypic appearances for stromal dystrophies: granular, lattice, and corneal. Such disorders in the stroma often extend to the anterior layers of the cornea, causing loss of visual clarity and can cause painful erosions [24].

2.1.4 Descemet's membrane

Descemet's membrane is a highly organized thin layer of ECM that contains mainly collagen and laminins. Its thickness grows from 3 μm up to 10 μm with age. It is continuously secreted from endothelial cells, thus, regenerative. Descemet's membrane serves as a barrier to separate stroma from endothelium for homeostasis. In addition, it helps support the corneal structure, maintains corneal transparency, and allows nutrient transportation from the endothelium [3,25,26].

Though the Descemet's membrane is regenerative, it has a poorer ability to repair mechanical trauma and infectious defects than the epithelial cells. Besides, as a product of the endothelial cells, it also suffers from endothelial dystrophies [26,27].

2.1.5 Endothelium

The endothelium is a single layer of cells forming the cornea's innermost surface. The endothelium cells are hexagonal in shape, forming a honeycomb-like mosaic from the posterior view. Unlike epithelial cells, endothelial cells are not regenerative [3,4,27]. Instead, they become larger to fill up the vacancy of dead cells along with aging, also thinning in thickness. A healthy human cornea has an average decrease rate of roughly 0.6% in endothelial cell density since adulthood. From birth, the cell density drops from 3000 to 4000 cells/mm^2 to approximately 2600 cells/mm^2. The thickness also decreases from 10 μm and stabilizes at about 4 μm in adulthood [3,4]. The endothelial cells are essential

in regulating fluid flow between the stroma and the aqueous humor. They keep the stroma hydrated and balance its ion level, maintaining its transparency and elasticity [4].

Like other parts of the cornea, epithelial cells can also suffer from dystrophy. Other epithelial diseases include bullous keratopathy, iridocorneal endothelial syndrome, post-traumatic fibrous down growth, glaucoma, and diabetes mellitus. The Descemet's membrane may also take collateral damage from these diseases due to its close relation to the endothelium [27]. Loss of endothelial function often causes stromal disorder as well, resulting in vision impairment [4,27].

Given the importance of good vision and the limited recovery capability of the ocular tissue, for any ophthalmic diseases, early diagnosis of these diseases' signs is vital for timely treatments. Pathological changes in the cornea can cause morphological changes in the cells. These changes usually start on a cellular level before it spreads to a wider range in surrounding tissues. However, it is hard to realize or visualize these changes before it is severe enough to impair a patient's vision. Therefore, having easy-to-use and high-resolution diagnostic tools is always desired in clinical applications.

2.2 Clinical modalities for in-vivo corneal imaging

Conventional imaging modalities used for clinical assessment of the human cornea are the slit lamp, the ultrasound microscope, the in-vivo confocal microscopy (IVCM) and anterior segment optical coherence tomography (OCT). A slit lamp focuses an optical beam of with adjustable height, width, and angle, allowing the examiner to visualize separately both the anterior and posterior segments of the eye [5]. This instrument poses low risk to the patient, it is easy to operate and has low cost, which makes it a standard tool that appears in almost every ophthalmic clinic. However, the resolution that it can provide is comparable to a handheld magnifying glass, which is far from achieving cellular level assessment [5]. Ultrasound microscopy employs ultrasound waves with frequencies in the range of 50 to 100 MHz, and it measures the speed of sound of the echoes returning from different depths in the cornea. It allows in-vivo cross-sectional view of the tissue at a high speed. The typical lateral and axial resolutions of conventional clinical ultrasound microscopy are about 50 um and 20 um respectively, which again, is not sufficient for cellular imaging. Besides, due to the poor penetrating ability of ultrasound in biological tissues, it can only reach tissues that are 4-5 mm deep, which limits its application in ocular anterior imaging [28,29]. One major disadvantage of ocular ultrasound is the requirement of physical contact between the imaging probe and the corneal epithelium and the use of

ocular gel to reduce the impedance mismatch between air and the epithelial surface, that make this technology invasive.

Another popular non-invasive technology for in-vivo ocular imaging is in-vivo confocal microscopy (IVCM). Evolved from the traditional microscope setup, it uses pinhole apertures to block the out-of-focus scattered light, dramatically improving the image contrast. Depending on the optical design and scanning approach, IVCM can be classified as: tandem scanning-based confocal microscopy (TSCM), scanning slit confocal microscopy (SSCM), and laser scanning confocal microscopy (LSCM). By using a high numerical aperture focusing lens, LSCM can achieve lateral resolution in the order of 1-2 um and an axial resolution of about 4 um and with a typical field of view (FOV) of 400 um x 400 um in real-time imaging [6,7]. IVCM has been proven very useful in diagnosing many corneal diseases with a cellular resolution: dry eye disease, corneal ectasia, dystrophies and degenerations, iridocorneal endothelial (ICE) syndrome, and infective keratitis [8]. However, during examinations, the operator has to adjust the position of the objective laterally and the depth of focus in the axial direction to obtain a volumetric scan [30], which results in a low image acquisition rate and long imaging sessions. Moreover, in most cases IVCM requires direct contact of the imaging probe with the corneal surface in order to generate images of high resolution and contrast [30,31], which is not as comfortable for the patient. In addition, the slow acquisition speed causes IVCM to suffer from image artefacts due to involuntary eye motion.

The small amplitude yet rapid motions of the eye are called saccades. Saccades can both be driven consciously or happen involuntarily. The amplitude of the saccades can vary from 3 to 15 degrees with a linear increase in peak angular velocity up to 700 degrees per second [32]. During visual fixation, involuntary eye movements can be classified into three types based on their scales, speeds, and patterns: drifts, tremors, and microsaccades [33]. Assuming a naturally relaxed state for a healthy patient, the primary type of saccade that affects the imaging quality is the microsaccades. Microsaccades are the unconsciously generated micro motion that occurs on top of the slow drift motion. They have amplitudes ranging from 0.01 degrees to 0.3 degrees and frequencies ranging 1-2 Hz [34]. Given their high speed and high frequency, microsaccades can cause blurs and distortions in ocular imaging, especially in real-time examinations. These motions can also affect signal accuracies in dynamic clinical applications, for example, Doppler imaging.

In the hope of suppressing the image defects caused by these involuntary motions meanwhile achieving high resolutions, an emerging tool has captured more attention of clinicians and scientists, the optical coherence tomography (OCT) technology. The following section briefly reviews various OCT methods, demonstrating their advantage in volumetric ocular imaging.

2.3 OCT technologies

2.3.1 OCT history

Optical coherence tomography (OCT) is an imaging technology that can acquire volumetric measurements of the sample based on low-coherence interferometry (LCI). LCI first appeared in measuring back-scattered light signals in optical fibers and integrated-optic systems in the 1980s, achieving sub-millimeter axial resolution, and was given the name of optical frequency domain reflectometry [35,36,37]. The technology was adapted with a two-dimensional scanning modality and used in biological tissue imaging in 1991 by Fujimoto's research group from MIT. It was also when the name optical coherence tomography was published for the first time [38]. Only within ten years of its emergence, OCT technology was investigated by multiple research groups and successfully utilized in in-vivo imaging of ocular structures, demonstrating its great potential in ophthalmic applications [39-43].

OCT measures the depth-dependent variations in the refractive index of the imaged tissue based on the optical path length difference between the reference arm and the sample target interface. In the early stage of OCT development, the length of the reference arm changes at a constant speed to match the time-of-flight of light in the sample optical beam that is reflected from different depths within the imaged object. Such a method is referred to as the time-domain (TD) OCT. TD-OCT has succeeded in achieving high-resolution images; however, the A-scan acquisition rate of is limited to a few kHz due to the mechanical scanning of the reference mirror. A single cross-sectional OCT image (B-scan) comprised of 1,000 A-scans and acquired with a TD-OCT system operating at 1 kHz would require acquisition time of 1 second (equivalent rate of 1 B-scan/sec). Therefore, microsaccades introduced imaging artefacts in the TD-OCT B-scans.

Significant improvement of the OCT image acquisition rate was achieved by the development of an alternative OCT design, Fourier-domain (FD) OCT. FD-OCT retrieves a depth scan by mapping the

signal along the wavenumber-space. It can be categorized into two distinct designs based on different spectrum interpretation strategies. The first is called spectral-domain (SD) OCT, also referred to as spectrometer-based OCT, where a dispersive element (spectrometer) records the spectrum from a broadband, continuous wavelength light source [10,44-47]. The second method is named swept-source (SS) OCT, where a rapidly tunable light source produces a narrowband spectrum that scans over a broad wavelength range [11,48]. In SD-OCT, signals from multiple scattering sources along the axial direction are recorded simultaneously; then, the depth information is decoded by applying a Fourier transformation on the recorded spectra. This way, SD-OCT systems do not require a mechanical scanning of the reference arm mirror, which greatly increases the OCT image acquisition rate. Moreover, because the light is utilized more efficiently, the FD-OCT design dramatically improves the image's signal-to-noise ratio (SNR) and acquisition speed. Studies have shown that FD-OCT offers a hundreds-fold increase in SNR compared to TD-OCT [49-52]. The first FD-OCT (SD-OCT type) was developed a few years after the TD-OCT publication [44], and the first in-vivo images acquired with SD-OCT were reported shortly after [45,46]. Over the past decades, SD-OCT has shown increasing popularity for clinical use, thanks to the advancement in light source and detector technologies.

2.3.2 OCT imaging modalities

OCT uses similar terminologies as ultrasound biomicroscopy in describing the image dimensions, given the similarity between LCI and ultrasonic imaging methods principles [53]. Suppose we use the cartesian coordinates to characterize the geometry of the acquired image. In that case, the light propagating direction is usually noted as the z-direction, and a single column of data in the z-direction acquired by the same beam is called an A-scan. Then the surface that is perpendicular to the z-axis is the x-y plane. A two-dimensional image of multiple A-scans from either x or y-direction is called a B-scan. We can obtain a volumetric image if we put multiple B-scans together, and the x-y plane cross-sectional view of the volumetric image is a C-scan, also known as an en-face image. In order to get a volumetric scan of a sample, the system needs to guide the imaging beam to cover an area in the x-y plane. In OCT imaging, there are three common scanning protocols, which are demonstrated in figure 2.1.

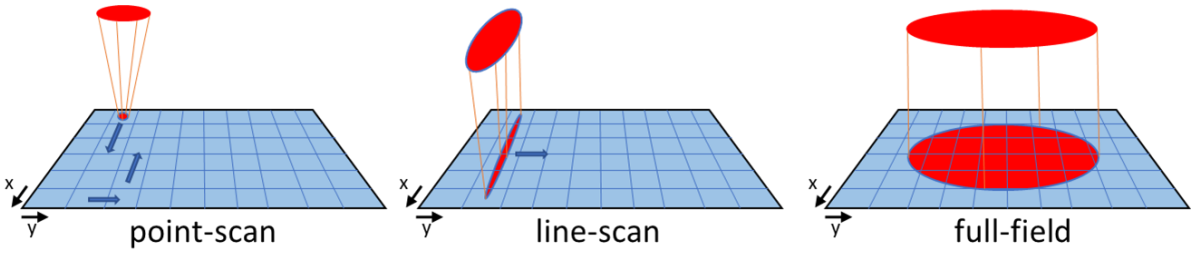

Figure 2.1 Schematic of three OCT imaging modalities: (A) point-scan, (B) line-scan, and (C) full-field.

The first modality is the point-scan design, where the imaging beam is focused isotropically to a circular shape in the x-y plane. Usually, a 2D galvanometric scanner pair can be used to guide the beam to cover a lateral area in a raster scan pattern. Besides, in applications where a probe is involved, i.e., endoscopic OCT, a 1D or 2D micro-electro-mechanical system can be used to provide the required flexibility and portability [54,55]. In these setups, one scan of the X mirror at one Y location will create a B-scan. Advantages of point-scan systems mainly arise from their simplicity. As it does not require any shaping of the beam, the majority of the system can be housed in optical fibers. Fiber's ductility allows easy adaption of OCT imaging to applications where mobility is necessary, for example, endoscopic OCT. It is also possible to integrate OCT imaging with other processing tools, like OCT-guided laser surgery [56] and inline coherence imaging in material manufacturing [57]. Moreover, the fiber can also serve as a confocal pinhole to reduce the noise from out-of-focus scattered light. However, on the other hand, the lengthy scanning distance by this scanning protocol unavoidably slows down the acquisition speed, which makes it suffer from defects caused by sample motions. Current state-of-the-art commercially available OCT devices can offer a maximum A-scan acquisition rate at about 200 kHz [58], which is still too slow to overcome the image artifacts caused by involuntary eye motions. Without considering the high cost of better light sources and detectors, research-grade broadband source OCT systems have achieved a speed of up to 400-600 kHz A-scan/s using high-speed CMOS cameras [59,60]. Research groups have also reported a 5.2-6.4 MHz axial-scan rate at a single spot with swept-source OCT setups using Fourier domain mode locked (FDML) lasers [61,62].

The other two modalities involve parallelization of the acquisition by capturing multiple A-scans at various lateral locations simultaneously. The extended lateral illumination also allows a higher maximum permissible exposure power over an area, guaranteeing high sensitivity under a high acquisition speed [63]. Line-scan (LS) or line-field (LF) OCT was first demonstrated in 1999 with a

broadband light source and spectrometer setup [64]. Using a line illumination, all A-scans for a single Y location will constitute the same B-scan and all A-scans belonging to that B-scan are acquired in parallel. Thus, in an LS-OCT system, the scanner only needs to sweep over in one lateral direction. However, a two-dimensional detector (area camera) is required in a spectrometer setup, as one side of the returning beam is occupied with spatial information, and spectral mapping must be extended to the other, orthogonal direction. Effective A-scan rates of above 500 kHz have been achieved using ultra-high-speed cameras [65,66].

Even faster scanning rates have been accomplished with swept-source LS OCT, where only a one-dimensional detector is used. The detector reads out one recording for each step of the spectral sweep, and then a complete B-scan is obtained after a full spectral sweep. LS SS-OCT has yielded a megahertz effective A-scan acquisition rate with high-quality results in in-vivo imaging [67]. Full-field OCT is adapted from LS SS-OCT technique by replacing the line detector with a two-dimensional one. The full-field illumination covers an area on the lateral plane; thus, a 3D volumetric scan can be acquired with one spectral sweep. It should be noted that a spectrometer setup or a 1D detector does not work with the full-field protocol, as both directions of the illumination contain spatial information, and there is no extra available dimension for interpreting the signals, either in the time-domain or spectral domain. Benefitting from its simultaneous vast area coverage, FF SS-OCT can reach a high effective A-scan rate up to nearly 40 MHz [68], however the spectral bandwidth (laser tunable range) is significantly narrower compared to that of CW light sources used in SD-OCT, which results in significantly lower axial resolution on FF SS-OCT systems compared to LS-SD-OCT [69].

The superior acquisition speed advantage of the parallel imaging modalities has resulted in increasing popularity in clinical studies. High-speed imaging is always desired in ophthalmic applications to eliminate the artifacts caused by eye movements, such as microsaccades and ocular drifts. Though these artifacts can be partially avoided and corrected by eye fixation or eye tracking algorithms, these methods also bring discomfort and prolongation in imaging sessions. Higher acquisition speed can also improve the digital resolution by capturing more A-scans without increasing the total acquisition time. In research, ultra-high-speed modalities are also favored in functional OCT studies. However, these parallelization designs also have noticeable downsides: 1. The increase in the scanning speed reduces the illumination and exposure time over one location, resulting in fewer photons being detected and a drop in sensitivities, which is valid for all OCT modalities [70]; 2. As the detector simultaneously receives multiple back-scattered signals from adjacent locations, there is a chance that a signal is

mistaken as its neighbors. Such artifact is known as spatial crosstalk and can be avoided using a spatially incoherent light source, such as a halogen lamp, a holographic diffusor, or a multimode fiber [70]; 3. A complex set of optics are usually required to shape the source beam to provide wide illumination in the parallel modalities, which is impossible to perform in optical fibers. Building the system in free space makes it exceptionally difficult for alignment. A free space system is also susceptible to environmental changes, making it hard though not impossible to adapt for clinical and industrial applications.

2.3.3 LS-OCT and Powell lens

Line-scan OCT modality splits the difference between point-scan and full-field methods and benefits from their advantages. The beam focuses on the sample imaging plane in one lateral direction; therefore, like in a point-scan system, it has a confocal gate in this direction. A slit can be placed on the returning route of the sample light to block the back-scattered signals those are out of focus. The source beam is shaped into an illumination line in the other direction to collect multiple A-scans at one time, making it more spatially stable along the line and less time-consuming to complete a volumetric scan.

A line-scan system requires a beam expander to form the line illumination on the target imaging plane. Commonly, a concave cylindrical lens is placed at the beginning of the system to serve this purpose. As a circular Gaussian beam transmits through the cylindrical lens, the beam diverges in the power direction of the lens while remaining unchanged in the non-power direction. Thus, an elliptically-shaped line beam with Gaussian intensity distribution in both axes is formed. However, this Gaussian-shaped line illumination also brings a potential image quality issue due to its uneven power distribution. When using an OCT system to image in-vivo or ex-vivo, the major signal is from the scattered light of the tissue. After taking imaging plane curvature and tissue absorption, the strength of the useful signals is often less than 0.1% of the incident light. Therefore, if the incident line illumination has a Gaussian distribution in its beam profile, the intensity at the edge of the beam diameter is about five times weaker than that at the FWHM. Hence, it would lead to poor signal strength at the two ends of the line, resulting in significant reduction of the image contrast.

A Powell lens is a type of conic aspherical lens known as a laser line generator. Similar to a cylindrical lens that only expands the incident collimated beam in one direction, a Powell lens can produce an output beam with a well-defined fan angle. Moreover, when a Gaussian beam passes through a Powell lens, it is enhanced to have a uniform intensity distribution in the expanding direction

[71]. Powell lenses have been adapted in several microscopy and sensor applications and are claimed to yield a better FOV than cylindrical lenses [72,73,74]. A LS-OCT utilizing a Powell lens for in-vivo imaging of biological tissue was reported recently [75]. However, the optical design of that system resulted in low spatial resolution (axial resolution of 2.0 μm and lateral resolution of 6.2 μm) and low sensitivity (system's SNR of 87 dB for 20 mW optical power incident on the imaged tissue and image acquisition rate of 3500 B-scans/sec).

Chapter 3 Theory

This chapter provides a brief overview of the theory of OCT. For a more detailed introduction to OCT technologies, please refer to reference [9], which is also the original source material for the content presented in this chapter.

3.1 Imaging principle of OCT systems

Optical coherence tomography technology (OCT) maps spatially dependent variations in the refractive index of biological tissues by detecting backscattered light from the locations in the imaged object where those variations occur. Because these changes are small, OCT uses interferometry to amplify the corresponding optical signals. The optical design for majority of the OCT systems is based on a Michaelson-Morley interferometer setup powered by a broadband light source, though some OCT systems are based on Mach-Zehnder design. Figure 3.1 illustrates the schematic of a typical OCT system. We assume the system is in free space and show only the essential components to simplify the theory without losing much of the generality. At the system's center, a beamsplitter splits the broadband light from the source into a reference arm and a sample arm. The sample arm guides the light onto the sample target, and the reference arm reflects the light with a terminating mirror. The returning light from the reference arm mirror reflection and backscattered from different depths in the imaged sample recombine at the beamsplitter and further propagate to the detector, producing an interference signal dependent on the path length difference between the two arms.

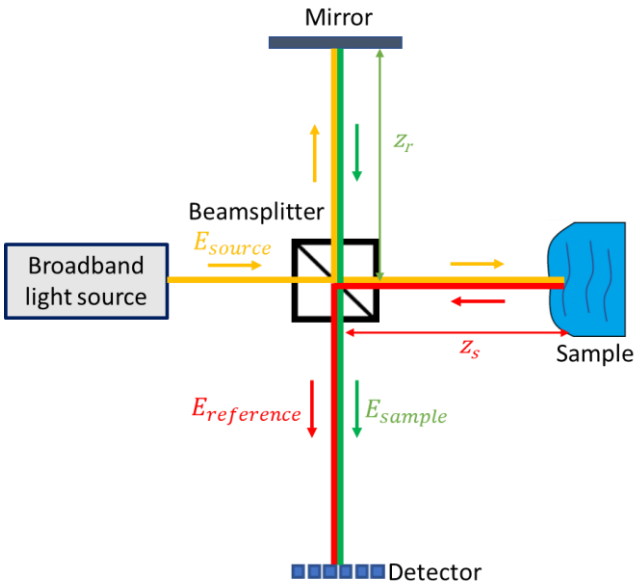

Figure 3.1 Schematic of a Michelson-Morley interferometer OCT setup.

Assuming a polychromatic plane wave traveling along the z-direction at time *t*, we can express the electric field of the broadband light source as:

$$E_{source}(k) = s(k)e^{i(kz-\omega(k)t)}$$
$$E_{source} = \int E_{source}(k)dk \qquad \text{Eq 3.1}$$

where k is the wavenumber, $\omega(k)$ is the angular frequency, and $s(k)$ is the wavenumber-dependent electric field amplitude. Though the specs of a light source are often given in wavelength, λ, or frequency, f, we use k as the independent variable in this equation as the final OCT signal will be interpreted in k-space. The fundamental relationships among these quantities are $k = \frac{2\pi}{\lambda} = \frac{2\pi f}{c} = \frac{\omega}{c}$, where c is the speed of light.

We can then write the returning sample and reference electric fields that reach the detector. First, we use $\rho_r(k)$ and $\rho_s(k)$ to represent the signal reduced power portion due to the beamsplitter transmitting and reflecting ratio. For a single mirror in the reference arm sitting at an optical path length of z_r, the electric field received by the detector is:

$$E_{reference}(k) = \rho_r(k)E_{source}r_r e^{i2kz_r} \qquad \text{Eq 2.2}$$

where r_r is the reflectance of the reference mirror and is assumed to be k-independent. The factor of 2 in the exponent part is from light travelling a round trip of the path length.

We can model the sample target to be a combination of n reflectors, each with an optical path length, $z_{s,i}$, and a scattering efficiency $r_{s,i}$. The overall scattering profile at optical path length z_s, can be written as:

$$r_s(z_s) = \sum_{i=1}^{n} r_{s,i}\delta(z_s - z_{s,i}) \qquad \text{Eq 2.3}$$

Thus, the returning sample electric field is:

$$\begin{aligned} E_{sample}(k) &= \rho_s(k)E_{source}e^{i2kz_s} \otimes r_s(z_s) \\ &= \rho_s(k)E_{source}\sum_{i=1}^{n} r_{s,i}\, e^{i2kz_{s,i}} \end{aligned} \qquad \text{Eq 2.4}$$

The sample and reference electric fields produce a photocurrent that is proportional to the time average of the square of sum of their field strength:

$$I(k) = \mathcal{R}(k)\langle|E_{reference} + E_{sample}|\rangle^2 \qquad \text{Eq 2.5}$$

where $\mathcal{R}(k)$ is the wavenumber-dependent responsibility of the detector. By substituting the expressions for $E_{reference}$ and E_{sample}, and integrating E_{source} over time, we end up with the time invariant form of the photocurrent:

$$\begin{aligned} \mathrm{I}(k) \propto S(k)&\left[R_r + \sum_{i=1}^{n} R_{s,i}\right] \\ &+S(k)\left[2\sum_{i=1}^{n}\sqrt{R_r R_{s,i}}\, cos(2k(z_r - z_{s,i}))\right] \\ &+S(k)\left[2\sum_{i,j=1,i\neq j}^{n}\sqrt{R_{s,i}R_{s,j}}\, cos\left(2k(z_{s,i} - z_{s,j})\right)\right] \end{aligned} \qquad \text{Eq 2.6}$$

Here $S(k) = \mathcal{R}(k)\langle|s(k)|^2\rangle$ is the time-averaged effective spectrum profile received by the detector. Several simplifications are made. First, we assume $\rho_r(k) = \rho_s(k)$. However, we should note that in practice, though a $50{:}\,50$ (reflecting (R): transmitting(T)) ratio is a common choice for beamsplitters,

$\rho_r(k)$ and $\rho_s(k)$ can be different depending on special beam splitting requirements. And even for $50:50$ (R:T) commercially available splitters, they always have different functions of k for transmission and reflection. Second, we place ${r_r}^2$ and ${r_{s,i}}^2$ with ${R_r}^2$ and ${R_{s,i}}^2$, which represent the power reflectivity and scattering efficiency of the field squared. Third, we use Euler's rule to express the complex exponential functions in trigonometric functions.

There are three components in this equation. The first component is called the DC term or the constant term, which is the sum of raw signals from the two arms and is not dependent on the optical path lengths. The second component is from the interference between the reference signal and the signal from each interface in the sample structure and is named the cross-correlation terms. The third component arises from the self-interference among the sample scattered signals and is referred to as the auto-correlation terms. As R_r is much greater than $R_{s,i}$ in general, the self-interference signals strength among $R_{s,i}$ is much weaker than the cross-interference between $R_r$and z_s_i, and the auto-correlation terms are negligible. Besides, the DC terms are not dependent on the optical path length at all. Therefore, our main interest is focused on cross-correlation terms. The total photocurrent strength of the cross-correlation terms over the full spectrum can be calculated as the integral over all detectable wavenumbers:

$$I_{cc} = \int I_{cc}(k)dk \qquad \text{Eq 2.7}$$

$$I_{cc} \propto 2\,\mathcal{F}_{k\to z}\{S(k)\}\sum_{i=1}^{n}\sqrt{R_r R_{s,i}}\left[2\left(z_r - z_{s,i}\right)\right]cos\left(2k_0\left(z_r - z_{s,i}\right)\right) \qquad \text{Eq 2.8}$$

where $\mathcal{F}_{k\to z}\{S(k)\}$ is the Fourier transformation of light spectral profile $S(k)$ from k to z space, which is also known as the coherence function of the source light, and k_0 is the center wavenumber of the spectrum.

3.2 Time-domain (TD) OCT and Fourier-domain (FD) OCT

Assuming the light source outputs a spectrum with Gaussian-like profile that has a center wavenumber of k_0 and a bandwidth of Δk, $S(k) \propto e^{-\left(\frac{k-k_0}{\Delta k}\right)^2}$. Substituting this spectrum into equation 2.8, the cross-correlation terms of the detected signal can be rewritten as:

$$I_{cc} \propto 2\sum_{i=1}^{n}\sqrt{R_r R_{s,i}}\, e^{-\Delta k^2 \left(z_r - z_{s,i}\right)^2} cos\left(2k_0\left(z_r - z_{s,i}\right)\right) \qquad \text{Eq 2.9}$$

This function appears as a wave packet that has a trigonometrical modulation with frequency proportional to k_0, inside a Gaussian-shaped envelop. This wave packet peaks when z_r equals to $z_{s,i}$, thus, depth information can be extracted from it. The signal interpretation is illustrated in figure 3.2 (A). The ability to distinguish signals from two different depths is governed by the full width at half maximum (FWHM) intensity of the envelop, which is known as the coherence length, l_c, of the light source, also used to characterize the axial resolution of the system.

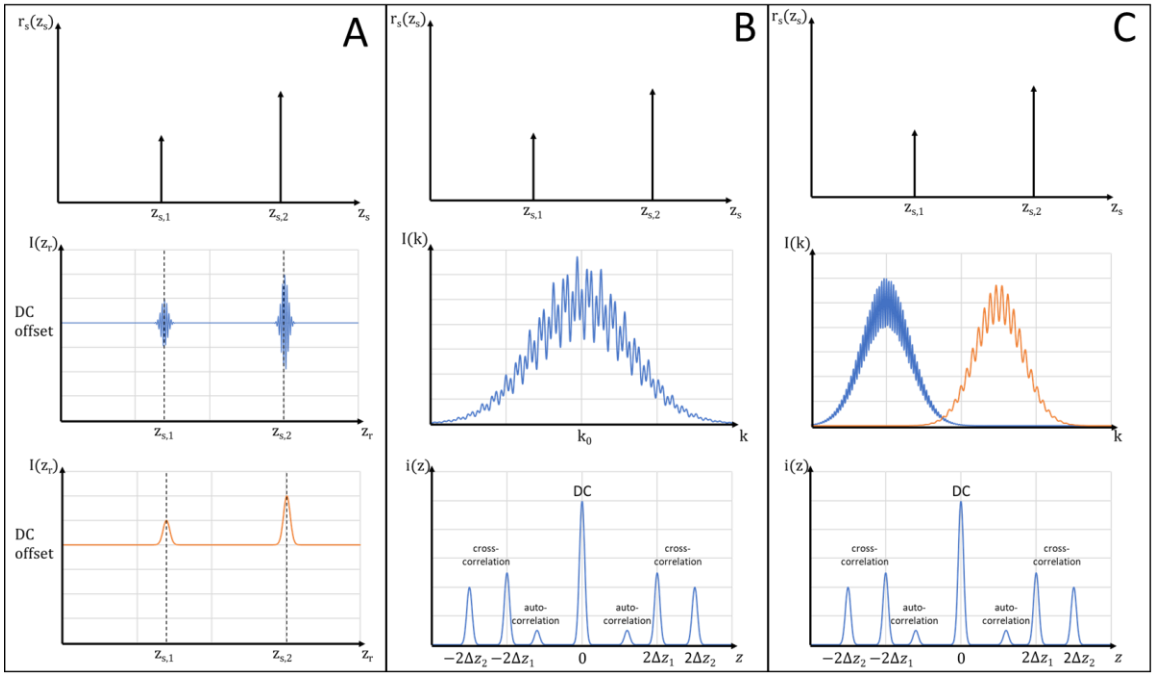

Figure 3.2 Signal interpretation from two scattering interfaces along one depth profile from (A) a TD-OCT and (B) a SD-OCT, and (C) a SS-OCT system.

In order to acquire signals from a range of depths of the sample with the highest resolution, z_r needs to change step by step at an interval of l_c to match the position of each scattering interface in the sample; this conventional method is called the time-domain (TD) OCT. Practically, a piezoelectric actuator is deployed to control this micro-motion for the reference mirror. For a total imaging duration time T for one depth scanning, the system will spend $\frac{l_c}{Z_{depth}}T$ at each step, where Z_{depth} is the desired scanning

depth inside the sample. The signal strength is linearly proportional to the exposure time at each depth; therefore, it has to stay for long enough time at each step for a good signal strength. On the other hand, the mechanical limitations of the actuator also restrict the data acquisition time for a full depth scan down to a few kHz at maximum.

An alternate method to extract the depth information is called the Fourier-domain (FD) OCT. The reference arm mirror is fixed in this method, and the signal described in equation 2.6 is measured in k-space. In k-space, the period of the trigonometric modulation is proportional to the difference between z_r and $z_{s,i}$, namely Δz. The larger this difference is, the more slowly this sinusoidal term oscillates. Besides, the change in $R_{s,i}$ will also result in a different amplitude for the oscillation. Thus, by operating a Fourier transformation onto the signal, we can extract intensity information of interfaces from multiple depth $z_{s,i}$ all at once. We can write the scattering profile along the depth as the real part of the Fourier transformation of the raw signal, $i(z) = \mathrm{Re}(\mathcal{F}_{k\to z}\{I(k)\})$, which gives:

$$\begin{aligned} \mathrm{i}(z) \propto \gamma(z) & \left[(R_r + \sum_{i=1}^{n} R_{s,i})\, \delta(z) \right] \\ & + 2\,\gamma(z) \otimes \left[\sum_{i=1}^{n} \sqrt{R_r R_{s,i}}\, \delta(z \pm 2\Delta z_i) \right] \\ & + 2\,\gamma(z) \otimes \left[\sum_{i,j=1, i\neq j}^{n} \sqrt{R_{s,i} R_{s,j}}\, \delta\left(z \pm 2\left(z_{s,i} - z_{s,j}\right)\right) \right] \end{aligned} \qquad \text{Eq 2.10}$$

The three components in these transformed forms inherit the same names from equation 2.4: the DC terms, the cross-correlation terms, and the auto-correlation terms. The DC terms center at $z = 0$ and is not Δz_i dependent. Locations of the delta function correspond to the optical path length difference between two interfaces in the cross and auto-correlation terms. These delta functions are broadened by convolution with $\gamma(z)$, the coherence function of the light source spectrum, which governs the resolution of each depth signal. As the distances among each sample interface pair are fixed, we can separate the cross-correlation terms from the other two terms by changing the optical path difference between the sample and the reference mirror. In practice, we subtract the dominating reference spectrum to remove most of the DC terms from the total measurement, which helps enhance the contrast of the true interference signal. The value of $(z_{s,i} - z_{s,j})$ is usually much smaller than the imaging range, so the auto-correlation terms are located very close to $z = 0$; the magnitude of $\sqrt{R_{s,i}R_{s,j}}$ is also too

small to make this signal strength comparable to the cross-correlation terms. The positive and negative $\Delta z_i \; and \; (z_{s,i} - z_{s,j})$arise from the complex conjugate from the Fourier transformation calculation and can be eliminated through data post-processing. Because FD-OCT systems measure the signal from all depth together, the signal strength is no longer limited by scanning step ratio $\frac{l_c}{z_{depth}}$ as in the TD-OCT system, which gives FD-OCT a tremendous advantage in the signal to noise ratio.

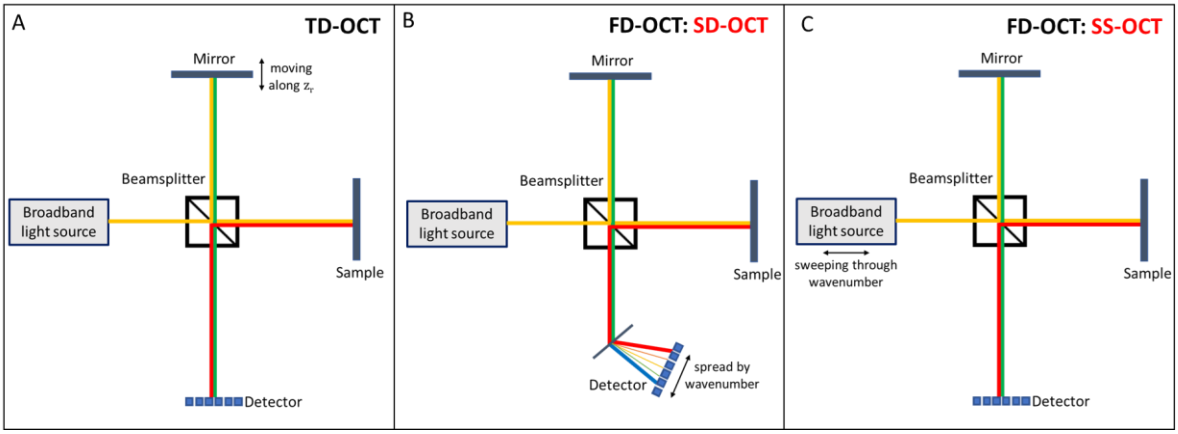

Figure 3.3 Schematics of (A) TD-OCT, (B) SD-OCT and (C) SS-OCT systems.

There are two variations in FD-OCT implementation based on different depth to k-space signal interpretation methods, which are demonstrated in figure 3.3 (B) and (C). One is the spectrometer-based FD-OCT, also known as spectral-domain or in short SD-OCT, which has a continuous broadband light source and employs a high-efficiency spectrometer to measure the spectral oscillations. The OCT signal is obtained through a continuous Fourier transformation (CFT) as the spectrum is dispersed and mapped on k-space continuously. The swept-source (SS)-OCT is another variation of FD-OCT, which utilizes a tunable narrowband light laser. The laser outputs a narrow spectrum whose center wavenumber is swept linearly through the total available wavenumber range Δk**.** Ideally, the sweeping of k should be constant over time; thus, only a single detector is required to record the evenly spaced spectrum in k-space, although a dual-balanced detector setup can be used for intensity fluctuation compensation. This method obtains depth-encoded OCT signals through a discrete Fourier transformation (DFT) on its individually recorded spectra. SS-OCT offers an even lower noise level detection than the spectrometer-based SD-OCT because the narrowband spectrum centered at each k has a much lower noise level. On the other hand, SD-OCT records the broadband spectrum all at once, where the noise accumulates through all k. However, SS-OCT systems heavily rely on light source

qualities. Current technology limits the choices of the central wavelength and the tunable wavelength range for OCT applications. In addition, a tunable laser is usually more costly than a broadband light source, such as a supercontinuum laser or a super luminescent diode.

3.3 SD-OCT parameters

3.3.1 Axial resolution

The axial resolution is defined as the ability to resolve two separated surfaces along the imaging beam axis. As the OCT signal is generated by low-coherence interferometry, its axial resolution is free of limitations from the optics or the beam geometry. Instead, it directly depends on the width of the coherence function, which is the Fourier transform of the source spectrum. Assuming a Gaussian shape for the spectral power density, $S(k) = S_0 \frac{1}{\Delta k\sqrt{\pi}} \exp\left(-\left(\frac{k-k_0}{\Delta k}\right)^2\right)$, we get a coherence function in the form of:

$$\gamma(z) = S_0 \exp(-(z\Delta k)^2) \qquad \text{Eq 2.11}$$

The axial resolution represents the coherence length of the light in a round trip and is determined of the full width at half maximum of this point spread function (PSF):

$$\Delta z = \frac{2\ln(2)}{\pi}\left(\frac{{\lambda_0}^2}{\Delta\lambda}\right) \qquad \text{Eq 2.12}$$

where λ_0 and $\Delta\lambda$ are the center wavelength the bandwidth of the source spectrum. This For imaging in other medium, the axial resolution is inversely proportional to the refractive index, n.

3.3.2 Lateral resolution and depth of focus

The lateral resolution is defined as the spot size of the focused beam assuming diffraction-limited conditions, which depends on the geometry of the focusing optics and the incident beam. When a parallel beam with a width of D enters the pupil of a lens with a focal length of f, the $1/e^2$ spot size at the focal plane, also known as the lateral resolution, can be written as:

$$\Delta x = \frac{\sqrt{ln2}}{\sqrt{2}\pi}\lambda\frac{f}{D} \qquad \text{Eq 2.13}$$

where lambda is the wavelength of the beam. As OCT uses a broadband light source, we commonly use the center wavelength, lambda0, to characterize the system. On the other hand, this focused beam's Rayleigh range, z_R, is used to determine the depth of focus (DOF). The DOF is the maximum displacement the focal plane can have along the light beam propagation direction while the lateral focus sharpness is still acceptable. The DOF limits the maximum depth the system can measure, which is given by:

$$b = 2z_R = \frac{\pi \Delta x^2}{2\lambda} = \frac{8\lambda}{\pi}\left(\frac{f}{D}\right)^2 \quad \text{Eq 2.14}$$

One thing noticeable is that both the lateral resolution and the DOF are positively related to the ratio of $\frac{f}{D}$. A dimensionless quantity called the numerical aperture (NA) can be used to represent this ratio. It is defined as:

$$NA = n\sin\left(tan^{-1}\left(\frac{D}{2f}\right)\right) \quad \text{Eq 2.15}$$

where n is the refractive index outside the lens. As $2f$ is normally much larger than D in magnitude, we can use a small angle approximation to simply this relationship to $NA \approx \frac{D}{2f}$. Now, we can rewrite the later resolution and the DOF as:

$$\Delta x = \frac{\sqrt{2ln2}}{\pi}\frac{\lambda}{NA} = 0.37\frac{\lambda}{NA} \quad \text{Eq 2.16}$$

$$b = \frac{2}{\pi}\frac{\lambda}{NA^2} \quad \text{Eq 2.17}$$

We should note that Δx is inversely proportional to b by a factor of NA, which brings a contradiction in OCT. As shown in figure 3.4, a greater NA will produce smaller focal beam spot size but shorten the DOF. The DOF can be improved with a smaller NA, but then the high lateral resolution is sacrificed.

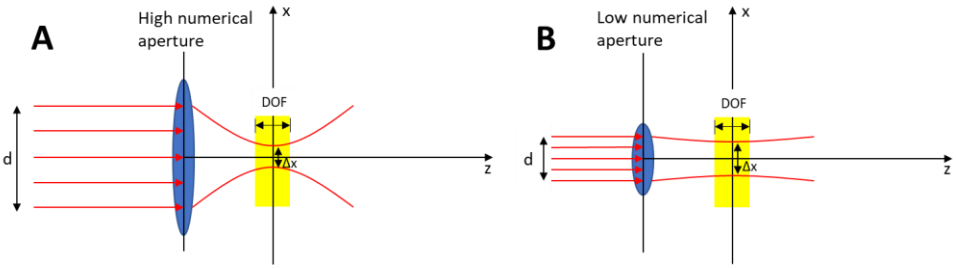

Figure 3.4 Schematic of beam propagation with (A) a large NA and (B) a small NA.

3.3.3 Field of view (FOV)

In a line scan OCT system, the FOV in the scanning and the line-illumination directions are decoupled. Figure 3.5 demonstrates a schematic of a typical sample arm design after the scanner. All lenses are placed following a 2f configuration with the adjacent lens and the scanner is one focal length away from L1. The scanner mirror tilts the beam with a scanning angle of θ. We can calculate the scanning direction FOV as:

$$FOV_{scanning} = 2f_1 \tan(\theta) \frac{f_3}{f_2} = 2f_1 \tan(\theta) M_{2,3} \qquad \text{Eq 2.18}$$

where f_1, f_2 and f_3 are the focal lengths of the lenses, $M_{2,3}$ is the magnification of the later lens pair.

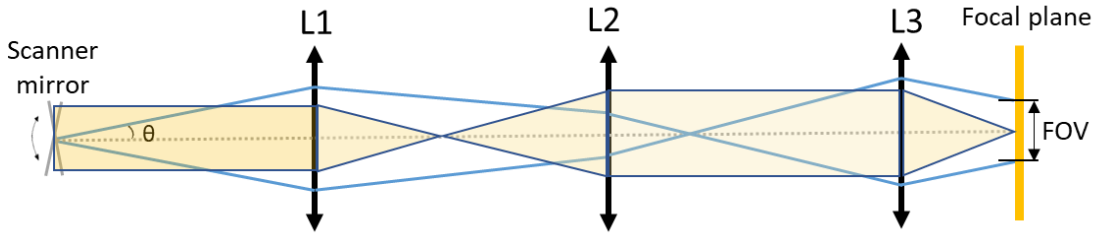

Figure 3.5 schematic of a sample arm scanner to focal plane light propagation. L1-L3, lens; θ, scanning angle; FOV, field of view.

The line-illumination direction FOV follows the rule of a wide-field microscopy setup:

$$FOV_{wide-field} = dM_{sample} \qquad \text{Eq 2.19}$$

Here, d is the beam size entering the sample arm and M_{sample} is the total magnification power in the sample arm. The FOV in this direction is also limited the pixel configuration of the detector:

$$n_p d_p = dM_{sample} M_{detector} \quad \text{Eq 2.20}$$

where n_p and d_p and the pixel number and pixel size of the detector, and $M_{detector}$ is the total magnification power in the detector arm. If nd is too small, the detector cannot capture the full returning signal from the sample.

The image pixel spacing describes how the physical dimensions are projected on a digital image. As OCT takes volumetric measurements of the sample, we have spacings the lateral directions, δ_x and δ_y, and for the depth direction, δ_z:

$$\delta_x = \frac{FOV_x}{n_{px}} \quad and \quad \delta_y = \frac{FOV_y}{n_{py}} \quad \text{Eq 2.23}$$

where FOV_x and FOV_y are the measurable physical FOV of the image in the lateral directions, and n_{px} and n_{py} are the number of data acquired in the two lateral directions to construct the digital image.

$$\delta_z = \frac{Z_{max}}{N/2} \quad \text{Eq 2.24}$$

Here, only half of the total spectral pixels are taken into calculation because the OCT depth signal are mirrored by the $z = 0$ axis due to Fourier transformation produced positive and negative conjugates. This shorten range is also known as the Nyquist limit. The signals from beyond this limit will be aliasing.

3.3.4 Depth scanning range

The depth scanning range is defined as the furthest signal an OCT system can detect along the axial direction before aliasing occurs due to reaching the Nyquist limit for the measured signal. From the cross-correlation terms in equation 2.6, we know that the signal oscillates as a sinusoidal function $cos(2k(z_r - z_s))$. For a total number of N pixels, we need $2\Delta k(z_r - z_s) \leq (\frac{N}{2})2\pi$ to make it still decodable. Thus, we have the maximum depth of scanning range, Z_{max}, as:

$$Z_{max} = \frac{N\pi}{2\Delta k} = \frac{N\pi}{2(k_{max} - k_{min})} \quad \text{Eq 2.21}$$

where k_{max} and k_{min} are the maximum and minimum readable wavenumber on the detector. We can write this quantity in terms of the wavelength for easier interpretation:

$$Z_{max} = \frac{N\pi}{2\left(\frac{2\pi}{\lambda_{min}} - \frac{2\pi}{\lambda_{max}}\right)} = \frac{N}{4\left(\frac{1}{\lambda_{min}} - \frac{1}{\lambda_{max}}\right)} \quad \text{Eq 2.22}$$

3.3.5 SNR and SNR roll-off

The strength of the photon current generated by the detector is described in Eq 2.6. Under the one sample interface scenario, we can write the powers from the reference arm and the sample arm as $P_r = \sqrt{R_r}S(k)$ and $P_s = \sqrt{R_s}S(k)$. The desired signal is only the cross-correlation term, for an interface at zero optical path delay position, the signal is given by:

$$I_{signal} = 2\sqrt{P_r P_s}\tau\frac{\eta}{h\nu} \quad \text{Eq 2.22}$$

where η is the total camera integration time for a full depth profile recording, ϵ is the quantum efficiency of the detector, h is the Planck's constant and ν is the light frequency; $h\nu$ together, is the photon quantum energy.

Assuming the reference arm power dominates the noise generation, the noise level variance can be derived from the DC terms of equation 2.6:

$$\sigma_{noise}^2 = P_r\tau\frac{\eta}{h\nu} \quad \text{Eq 2.23}$$

Then, we can write the SNR as:

$$SNR = \frac{{I_{signal}}^2}{{\sigma_{noise}}^2} = \frac{\eta P_s \tau}{h\nu} \quad \text{Eq 2.24}$$

Usually, we use the central frequency ν_0 and the corresponding quantum efficiency η_0 to characterize the theoretical SNR for the system. However, one should always remember that the SNR is wavelength dependent as the quantum efficiency is also a function of wavelength and it varies a lot among different detectors.

The SNR of an OCT system varies through the depth of scanning range. The signal strength decreases with an increasing depth as a result of finite spectral resolution and power loss from light attenuation. This phenomenon is referred to the SNR roll-off, which is a convolution of a rectangular function of the finite pixel size [51].

3.3.6 Dispersion compensation

Dispersion is the phase distortion of the OCT signal when it passes through different material compositions, which can degrade the axial image quality. For instance, dispersion in OCT will create a chirp in the fringe pattern which in tun will alter the magnitude and shape of the PSF, reducing the magnitude and cause asymmetry in its shape. It is crucial that dispersion is carefully compensated to achieve high resolution in OCT imaging [76]. Dispersion mismatch between the 2 arms of the OCT interferometer can be compensated by using either a hardware and or a numerical method, or combination of both. Hardware approaches use BK7 glass cylinders or pairs of prisms to compensate for the low orders of dispersion mismatch. Software approaches determine dispersion induces phase non-linearity and compensate it using numerical methods. This approach allows for compensating higher orders of dispersion mismatch caused by use of complex optical elements such as microscope objectives or doublet achromat lenses. [77,78]. By taking the dispersion effect into account, we can add an extra term in the cross-correlation terms from equation 2.6, which represent the OCT signal that reaches the camera:

$$S(k)\left[2\sum_{i=1}^{n}\sqrt{R_r R_{s,i}}\,cos\left(2k\left(z_r - z_{s,i}\right) + \beta(n,k)\right)\right] \qquad \text{Eq 2.25}$$

where $\beta(n,k)$ is the propagation constant. For simplicity, we assume a uniform material composition along the path, and the propagation constant has a form of Taylor expansion around the center wavenumber:

$$\beta(k) = \beta(k_0) + \frac{d\beta}{d\omega}|_{\omega_0}(k-k_0) + \frac{1}{2}\frac{d^2\beta}{d\omega^2}|_{\omega_0}(\omega-\omega_0)^2 + \cdots + \frac{1}{n!}\frac{d^n\beta}{d\omega^n}|_{\omega_0}(\omega-\omega_0)^2 \qquad \text{Eq 2.26}$$

This propagation constant is not dependent on depth in itself; instead, it applies the same phase distortion to all measurements throughout a depth scan. The first step to dispersion compensation in OCT systems is from the hardware aspects. Due to different functionalities, the sample arm and the reference arm do not necessarily contain identical optics. Commonly, additional BK7 glass is added to the arm with a shorter optical path length; in retinal imaging, a water cell is used in the reference arm to mimic the eye's anterior chamber. However, hardware compensation is never perfect. Further

numerical compensation can be performed for better correction in postprocessing, where a phase mask is created:

$$\Phi(k) = -a_2(\omega - \omega_0)^2 - a_3(\omega - \omega_0)^3 - \cdots - a_n(\omega - \omega_0)^n \qquad \text{Eq 2.27}$$

where a_n is an adjustable constant. In SD-OCT, the fringe pattern that contains the phase information is directly available for access, which makes it much easier than TD-OCT for numerical compensations. Higher order compensation will give better result, but the correction effect also becomes less prominent. Normally, 5th order adjustment in a_n will give good enough result.

3.4 Powell lens

Like a cylindrical lens, a Powell lens also has a curved roof and a flat bottom. The difference is, the lens roof in the power direction follows an aspherical curve which can be described as:

$$Z = \frac{cr^2}{1+\sqrt{1+(1+k)c^2r^2}} \qquad \text{Eq 2.28}$$

where k is the cone coefficient of the quadric surface, c is a curvature parameter, and r is a position in the radial direction with respect to the central axis of the Powell lens.

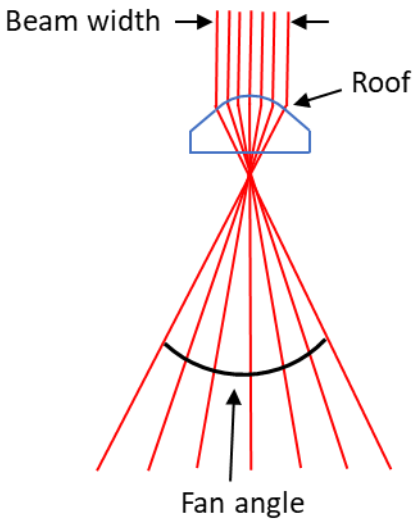

Figure 3.6 Schematic of a Powell lens

When a circular collimated beam is incident on the curved surface of the Powell lens (roof), it converges rapidly, then is refracted through the flat bottom surface and expanded with a fan angle in one direction. This generates a rectangular beam the intensity profile of which in the unchanged lateral direction is still Gaussian but has a quasi-uniform distribution along the expanded longitudinal direction.

Chapter 4 Optical Design of the PL-LS-SD-OCT System

4.1 Powell lens modelling in ZEMAX OpticStudio

The Powell lens we use in the system is from Laserline Optics Canada, which works with a 3 mm diameter beam and produces a fan angle of 5 degrees. Using the CAD model provided by the company, we extracted the key specs of the Powell lens and re-constructed the lens in the optical simulation software ZEMAX OpticStudio (Zemax LLC.). First, an aspherical curve described by equation 2.28. is fitted onto the roof surface of the Powell lens. The fitted curve radius and conic value are 12.125mm and -139.894, respectively. The company provides other essential information that the lens is made of N-BK7 glass without any coating, and the total thickness is 8.9 mm. The above constants allow us to do ray simulations of the Powell lens and its interactions with the other system components whose models are already available in the ZEMAX database.

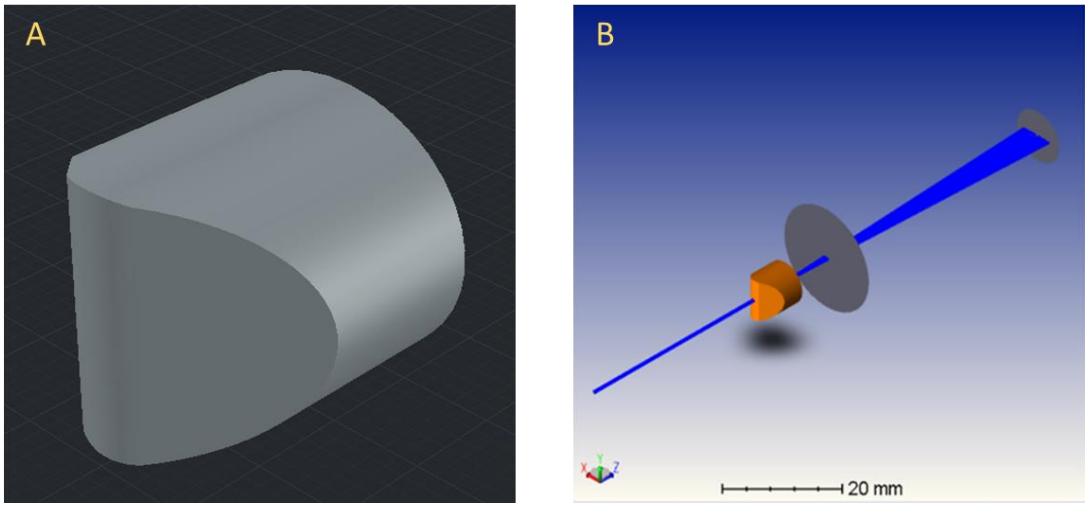

Figure 4.1 (A) reconstructed Powell lens CAD model in SolidWorks (Dassault Systems); (B) Zemax ray simulation with the 3D rendered Powell lens models using the fitted values.

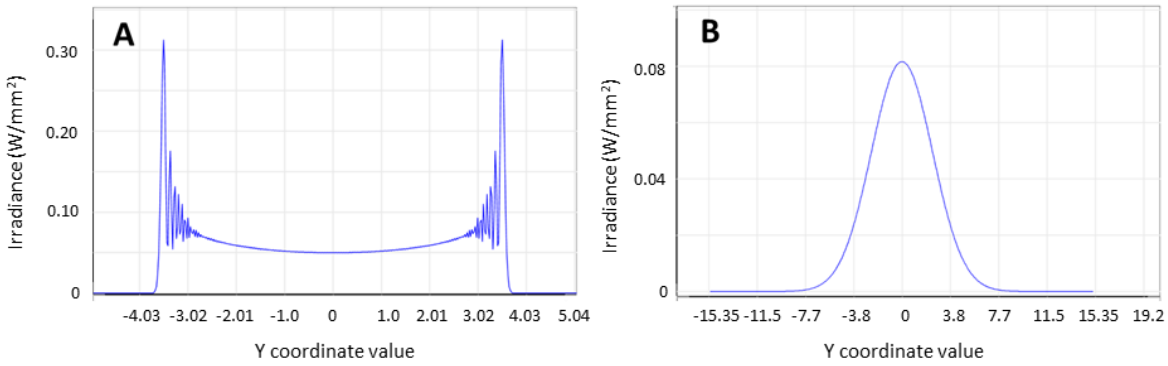

Figure 4.2 Simulated beam profiles of a (A) 10-degree Powell lens and a (B) f=75mm cylindrical lens when an incident beam with 3.2mm width is expanded by 3 times at the image plane.

Figure 4.2 compares the beam profiles after a 10-degree Powell lens and a 75 mm focal length cylindrical lens in ZEMAX simulations. The incident beam is a Gaussian beam with a width of 3.2mm, which matches the outputs of the collimator we are planning to use in the system, and the total power of the input beam in this simulation is set to 1W. Unless further notice, the same beam width, and power setting will be used in simulations for the following part of the thesis. The beam profiles in the expansion direction at the image plane are taken when the beam is enlarged twice. As expected, the Powell lens spectrum is more uniform than the cylindrical lens' Gaussian-shaped one, though strong fluctuating sidelobes are observed near the edges. Above 80% of the total cross-sectional power falls within the 80% beam width range. The power ratio from the 80% beam width position to that from the center is 1.31.

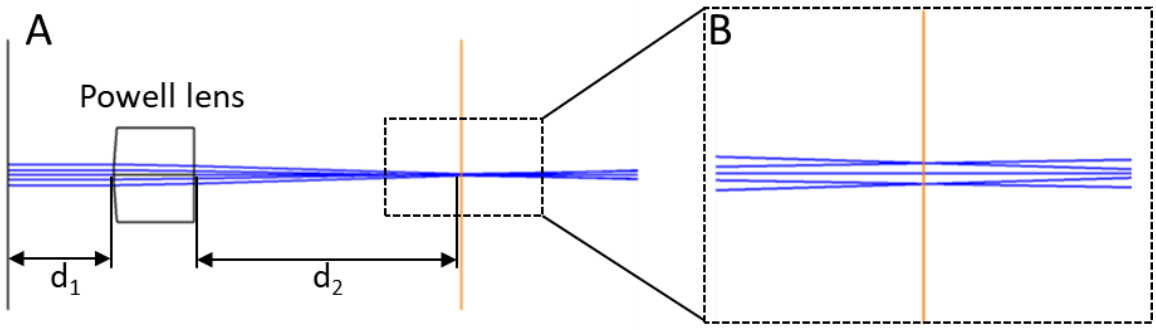

Figure 4.3 (A) Collimation beam focusing by the Powell lens. d_1, distance from the source aperture to the Powell lens roof surface; d_2, distance from the Powell lens back surface to the 'focus'; (B) Zoomed in view of the ‘focus’ region.

One thing that should be noticed is that a clear focal point cannot be identified when the beam converges after passing through the Powell lens, which is shown in figure 4.3. This behavior raises concerns that a Powell lens might not work well with other doublet lenses with a well-defined focal point. To understand the interactions between the Powell lens and other lenses, we did simulations on the Powell lens and a cylindrical lens pair before designing the Powell lens-based LS-OCT system.

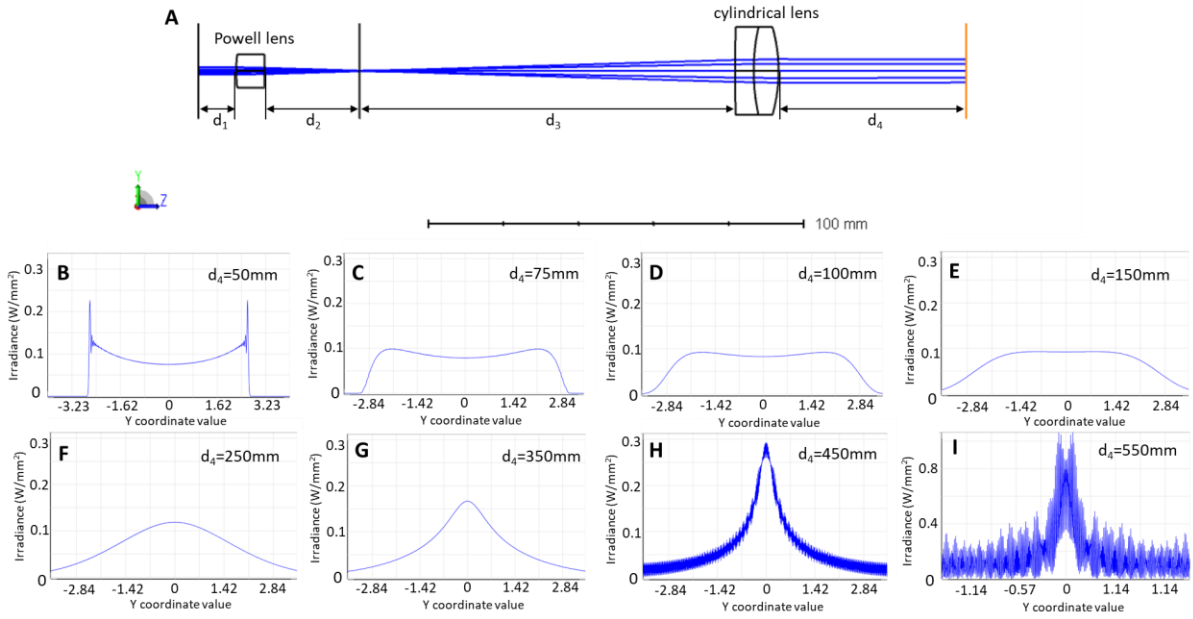

Figure 4.4 (A) 3D layout of a 10-degree Powell lens and f=75mm cylindrical lens pair simulation. d_1 and d_3, same as defined in figure 4.3; d_3, distance from the Powell lens 'focus' to the cylindrical lens front surface; d_4, distance from the cylindrical lens back surface; (B-I) Beam profile after lens pair at various distances from the cylindrical lens back surface. From B to I, d_4 = 50mm,75mm, 100mm,150mm, 250mm, 350mm, 450mm, and 550mm.

Figure 4.4 (A) shows the 3D layout of this simulation. As the Powell lens does not have a well-defined focus, the cylindrical lens is placed at one back focal length away from the narrowest converging point after the Powell lens. Further position adjustments are made to achieve the best parallelity between the beam edges in the first post 50mm propagation. The image plane gradually moves away from the cylindrical lens, and the corresponding beam profiles at different positions are demonstrated in figure 4.4 (B)-(I). As shown in figure 4.4 (B), the beam still has a typical Powell lens horn-shaped profile similar to figure 4.2 (A) at 50mm after the cylindrical lens. However, from figures

3.4 (B) to 3.4 (F), the beam starts converging towards the center and turns into a Gaussian-like shape as the distance increases to 250 mm. Finally, the beam keeps converging, and the profile becomes fully corrupted with intense fluctuations. The uniformity remains acceptable below d_4 = 100 mm. This will be well sufficient for corneal imaging applications, where the required scanning range is under 2 mm.

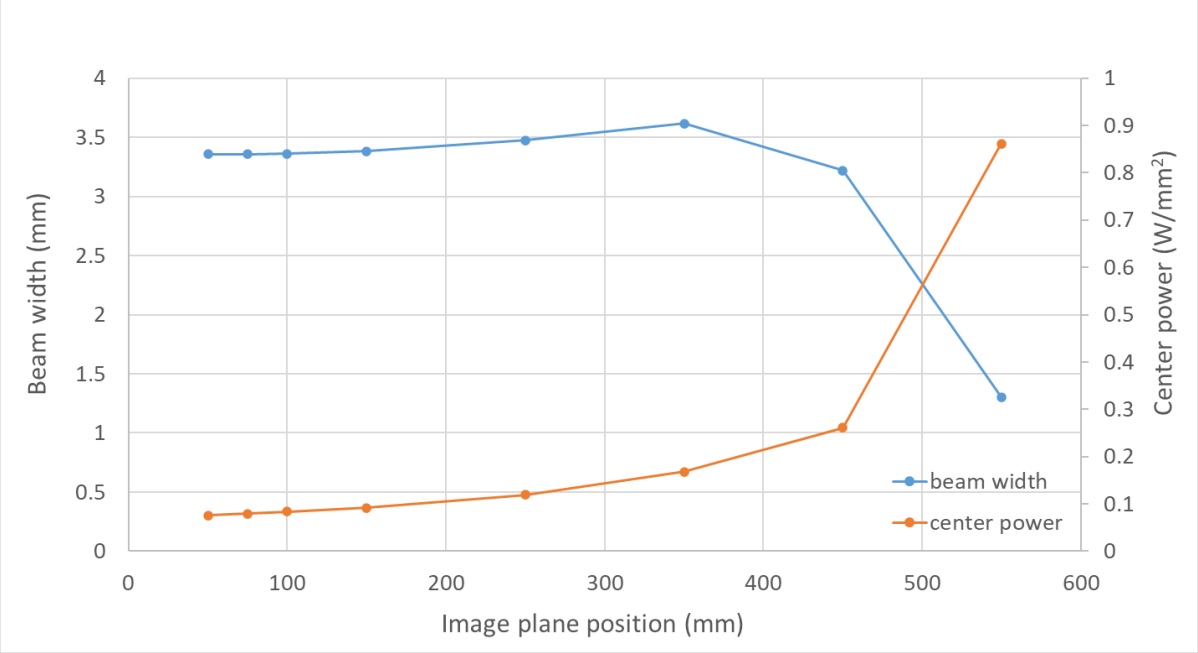

Figure 4.5 Plots of the width and the center power of the beam at different distances, d_4, from the Powell lens and cylindrical lens pair.

The beam width and center power information from the same simulation are extracted and plotted in figure 4.5. With the increase in the distance, the beam grows slightly more expansive at the beginning but drops quickly after it passes d4 = 350 mm. The power level at the center continuously rises at an increasing rate. The results from this lens pair simulation evidently demonstrate the instability of the beam, suggesting that a telecentric pair cannot be built from a Powell and a spherical lens. This means that the traditional Michelson interferometer-like OCT setup might not work well with a Powell lens.

For a spatial domain OCT system, either a fiber-based one or a free space one, there is only one beamsplitter at the system's center that divides the source beam into the reference arm and the sample arm. The same beam profile from the source arm will pass on to both the reference and the sample arms. One of the critical functions of the reference arm is that its path length must be adjustable to match the path-length of the light in the sample arm in order to generate interference pattern. The beam

profile in the reference arm should remain unaltered, therefore, it is necessary to have a perfectly collimated beam in the reference arm to fulfill this requirement. Suppose we were to use a cylindrical lens as the beam expander in the line-scan system. In that case, we could place another cylindrical lens in the reference arm to form a telecentric pair to bring the expanded beam back to collimation. However, as mentioned above, a Powell-cylindrical lens combination does not produce a collimated beam (fig. 3.5). Therefore, it is necessary to split the source beam at the very beginning and let the reference beam bypass the Powell lens. A detailed design and description of the system will be demonstrated in the next section.

4.2 Powell lens LS-OCT system

Figure 4.6 shows a schematic of the Powell lens LS-OCT system. The light in the scanning direction of the system, which is horizontal to the platform, is defined as the x-direction beam; and the light in the line illumination direction, which is vertical, is defined as the y-direction beam. In addition, z-direction will be used to describe the light propagation direction. The light source is a supercontinuum laser (SuperK, NKT Photonics) that has an emission spectrum from ~ 400 nm to ~ 1600 nm. A custom filter unit comprised of multiple low-pass, high-pass and ND filters is used to cut out a spectral band centered at 760 nm ±100 nm that is used in this project. An achromatic doublet (AC127-019-B, Thorlabs) was used to generate a collimated beam with a 3.2mm 1/e^2 width from the fiber output after the filter unit. The system design is based on a Mach-Zehnder interferometer. To solve the Powell lens spectrum issue in the reference arm discussed in the previous section, a beam splitter is placed right after the collimator to split the source light into two beams. One beam goes into the sample arm and passes through the Powell lens, and the other beam enters the reference arm and is free of the Powell lens effect. A 30:70 (R:T) beamsplitter BS1 (BS020, Thorlabs) is chosen to allow more power into the sample arm and improve signal strength.

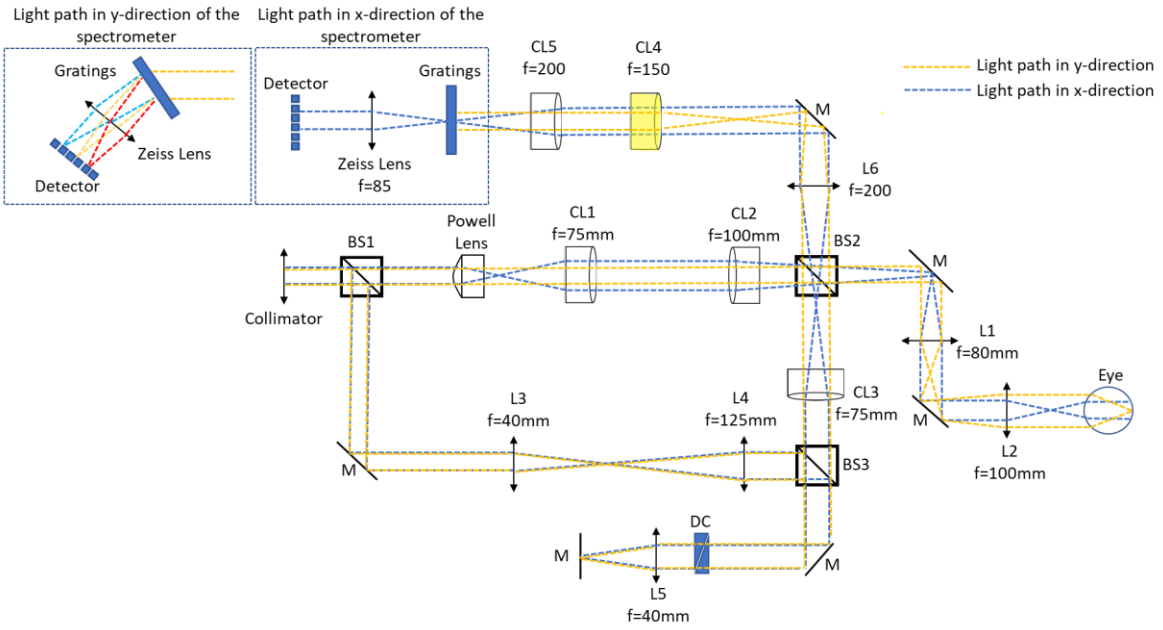

Figure 4.6 Schematic of the LS-OCT system. BS, beamsplitter; CL, cylindrical lens; L, spherical lens; GS, galvanometer scanner; M, mirror; MO, microscope objective; TS, translational stage; DC, dispersion compensation unit; ND, neutral density filter.

The beam is first expanded in the sample arm by the Powell lens PW (LOCP_8.9R05, Laserline Optics Canada) to create the uniform line illumination in the y-direction. The light then passes through a cylindrical lens telecentric pair, CL1 (ACY254-075-B, Thorlabs) and CL2 (ACY254-100-B, Thorlabs), with a magnification ratio of 1.33. After that, the beam transits through a 70:30 (R:T) beamsplitter BS2 (BS023, Thorlabs) and focuses onto the yz-plane of a 1D galvanometer scanner (GVS011, Thorlabs) that scans it in the x-direction. Finally, another telecentric pair composed of two spherical doublets, L2(AC254-080-B, Thorlabs) and L3(AC254-125-B, Thorlabs), magnifies the beam by a 1.25 ratio and guides the beam to the microscope objective (M Plan APO NIR 10x, Mitutoyo). At the focal plane, the line-shaped beam is 1.05 mm long and has a total incident power of ~2.4mW.

In the reference arm, the beam reflected from BS1 undergoes 3x expansion through a telecentric pair, L3 (AC254-040-B, Thorlabs) and L4(AC254-125-B, Thorlabs). In addition, a 50:50 beamsplitter BS3 (BS020, Thorlabs) reflects the beam to lens L5, which further focuses it onto the reference mirror. This mirror and L5 are mounted on two translational stages, which allow us to adjust the reference signal path length and the spectral shape of the reflected beam. By bypassing the Powell lens, the beam collimation is maintained before entering L5; thus, the beam profile remains intact when L5 and the

mirror move along the path. After the returning beam passes through BS3 again, a cylindrical lens CL3 (ACY254-075-B) shapes the circular beam into a line in the y-direction. A pair of BK7 glass prisms are placed in front of L3 to allow for hardware dispersion compensation. Reflective neutral density filters (ND filters, Thorlabs) with the desired optical density are mounted before L3 to control the reference arm signal intensity.

The reflected signal from the reference arm and the scattered light from the sample interfere at BS2 and propagate coaxially though the detector arm. The former part of the detector arm contains a series of lenses: a spherical doublet L6 (AC254-200-B, Thorlabs) and two cylindrical lenses, CL4 (ACY254-150-B) and CL5 (ACY254-200-B), that are oriented in x and y direction respectively. The dual-cylindrical lenses pair was firstly used by Sabesan's research group, enabling control of the x and y direction magnification separately [12]. Each of the cylindrical lenses forms a telecentric pair with L6 in its own power direction. The latter part is a custom spectrometer that is composed of a volume phase holographic grating (1200l/mm @ 840mm, Wasatch Photonics), a camera lens (Planar T* 1.4/8.5 ZF, Zeiss), and a high-speed CMOS camera (J-PRI, AOS Technology AG). The camera detector has a 2560 × 1920 rectangular pixel sensor with a pixel size of 7.8 × 7.8 um2, which can run at a maximum frame rate of 2000 fps when all pixels are armed. The grating disperses the spectrum in the x-direction, utilizing all the 2560 horizontal pixels in order to ensure that the spectral resolution of the spectrometer is not the limiting factor for the axial OCT resolution, as well as provide the maximum OCT scanning range. The spatial signal is projected vertically onto ~650 pixels; however, only the central 550 pixels are used when imaging due to the sidelobe fluctuations in the Powell lens spectrum. With a 2560 × 550-pixel configuration, the camera can run at the maximum speed of 6400 fps.

All doublets (L1-L6, CL1-CL4) are achromatic and anti-reflection (AR) coated for 650 nm-1050 nm. The beamsplitters (BS1-BS3) are all non-polarizing and AR coated for 700nm-1100nm. It should be noted that, though our spectrum goes below 700 nm to 660 nm, the transmission and refection efficiency of the beamsplitters at 660 nm still remains 70-80% of that within the 700 nm -1000 nm range. This will cause some, but not significant loss of the signals in the lower end of the spectrum. The microscope objective is NIR corrected, and the camera lens is also optimized for NIR transmission. All mirror surfaces, including the scanner, have silver protections.

4.2.1 Sample arm

The major components of the sample arm include the Powell lens, two cylindrical lenses, two spherical lenses, and the microscope objective. The microscope objective uses a paraxial lens setting in the simulation as the detailed lens configuration is not given from the manufacturer. The beamsplitter (BS2) and the scanner are not included in the ZEMAX simulation, as they should not alter the beam profile. Figure 4.8 (B) shows the irradiance projection when the image plane is at the exact focal point of the objective. After the objective, the beam is focused in the x-direction, but remains parallel in the y-direction. At the focal plane of the microscope objective (when s_6 = the objective focal length), the simulation shows the widths of the illumination line in the x and y directions and the x-direction Rayleigh length as 3.8 um, 0.65 mm, and 15 μm. In the x-direction, the beam receives a 1.56 magnification before entering the objective. The microscope objective has an effective focal length of 20 mm. By using equation 2.15, and 3.2 mm as the starting $\frac{1}{e^2}$ beam width, the theoretical beam width at the focus and the Rayleigh length can be calculated to be 3.82 μm and 15.3 μm, which agrees with the simulated value. As discussed in section 3.1, the Powell lens has no well-defined focal length, and its output beam does not follow a Gaussian behavior. Therefore, we want to see how the beam changes in the y-direction as it propagates through its focus in the x direction. Figures 4.8 (A) and (C-F) show the cross-Y beam profile at 0 mm, ±25 mm, and ±50 mm locations from the x focal point. The shape of the beam changes but the intensity uniformity and the beam length do not very much. The drop in intensity at further distances is expected because the beam also expands in the x-direction when it's further away from the focus. These results from the simulation suggest this setup should be able to provide a steady and uniform line illumination.

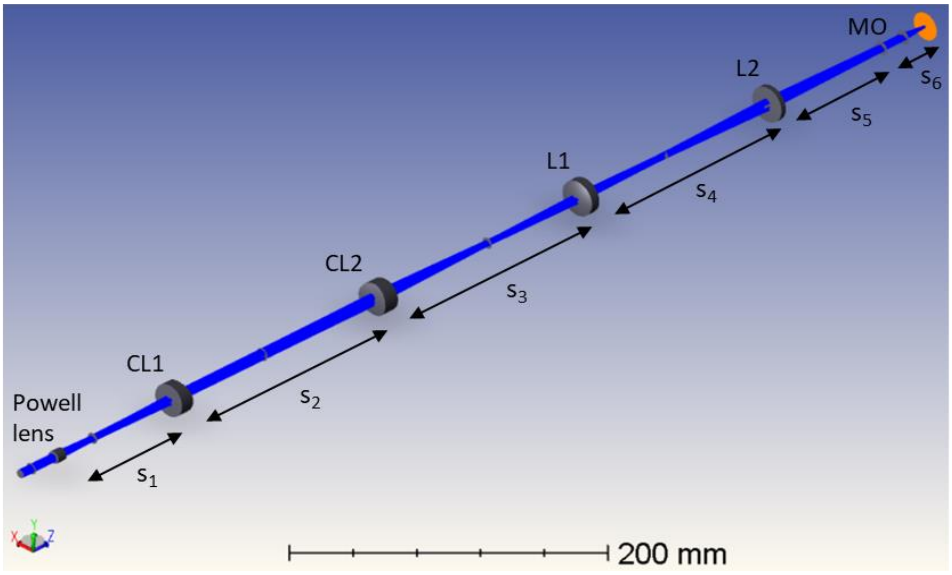

Figure 4.7 3D layout of sample arm optics in ZEMAX simulation. s_1- s_5, distances between two adjacent lens surfaces; s_6, distance of the imaging plane from the objective.

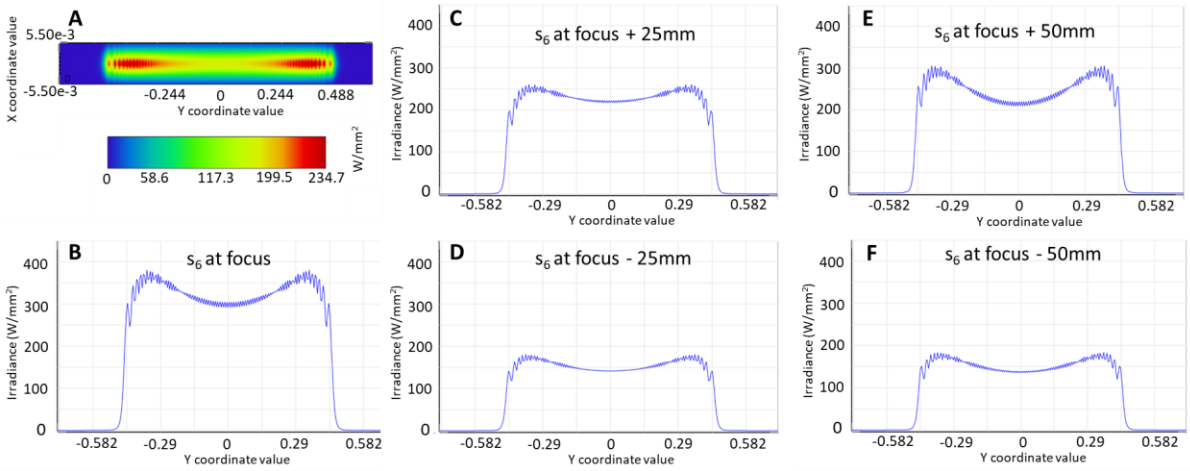

Figure 4.8 (A) Cross-Y beam profile at the focus. (B) Irradiance diagram of the beam at the focus. (C-F) Cross-Y beam profile at s_6 = focus ±25 μm and ±50 μm.

Last but not least, though the overall profile looks uniform, there are still intensity fluctuations near the edges of the line, which can cause a potential issue in the signal quality at the edges. The intensity fluctuation on the 20% edge is about 15%, comparing to <5% in the 80% center of the total profile. If

we block the spiky sidelobes, 80-90% of the central beam can remain of good quality, which is still better than a Gaussian illumination. We can cut the sidelobes by only utilizing 80% of the detector pixels in the vertical direction, which can help reduce the file size and boost the system saving speed.

4.2.2 Reference arm

For optimal interference, ideally, the reference and sample beams should have the same shape and size, overlap spatially by 100% at BS2 and continue to propagate coaxially to the camera sensor. Furthermore, the reference optical beam should be a collimated Gaussian beam for section of the reference path to allow for smooth adjustment of the reference pathlength to match the pathlength of the sample beam in order for the 2 beams to interfere at BS2. Any pathlength adjustments of the reference arm should not cause changes to the beam profile. As the combination of the Powell lens and the 2 cylindrical lenses does not allow for collimation of the optical beam, the system's optical design was based on Mach-Zehnder interferometer to decouple the reference and sample beams at BS1 and allow for the Powell lens to modify only the sample beam. A telecentric pair of achromat doublet lenses (L3 and L4) and a cylindrical lens (CL3) are used to generate an elliptically shaped reference bean at BS2. The magnification ratio of the telecentric pair was chosen so that the length of the elliptical line of the reference beam is >2x larger than the length of the rectangular line of the sample bean reflected off the imaged object when the 2 beams overlap at BS2 Taking 0.65mm as the line length returning from the sample, the beam will be 9.4mm long at L6. The current choice of focal lengths for L3, L4, and CL3 can produce a 26.6mm Gaussian-shaped line at L6. A variable slit is placed after CL3 to crop excess light from the larger reference beam. The center 9.4/26.6 portion of the reference Gaussian-shaped beam can offer enough uniformity to produce a steady interference throughout the sample signal length. In addition, the light source can provide sufficient power to the reference arm to compensate for the power loss from cropping the beam. Mirror M3 in the reference arm is mounted on a miniature translation stage to allow precise alignment of the mirror at the focal plane of lens L5. Both M3 and L5 are mounted on a large, manual translation stage to allow for smooth adjustment of the reference beam pathlength.

4.2.3 Detection arm

The detection arm of the PL-LS-SD-OCT system is comprised of the following optical elements: achromat doublet L6, cylindrical lenses CL4 and CL5, volumetric holographic grating (1200 line/mm, Wasatch Photonics), camera lens (Planar T* 1.4/8.5 ZF, Zeiss) and a high-speed CMOS area camera

(J-PRI, AOS Technology AG) with 2560 × 1920 pixels sensor and 7.8um × 7.8 μm pixel size. The rotational angle for the grating is calculated using the fundamental diffraction theory for a double slit.

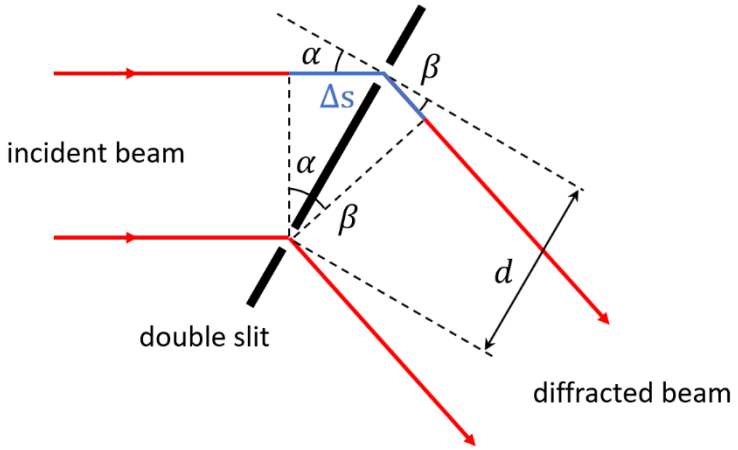

Figure 4.9 Schematic of ray diffraction by a double slit.

Figure 4.9 shows a schematic of double-slit diffraction. Alpha and beta are the incidence and diffraction angles, Δs is the path length difference between the two rays, and d is the separation between the two slits. The path length difference can be written as a function of the other quantities and the diffraction order n:

$$\Delta s = d(\sin\alpha + \sin\beta) \qquad \text{Eq 3.2}$$

We set n=1 and delta lambda as one ray wavelength for a first-order constructive pattern. For a typical spectrometer setting, we choose beta equaling alpha. Thus, we can rearrange the equation to be:

$$\alpha = sin^{-1}\left(\frac{\lambda_0}{2d}\right) \qquad \text{Eq 3.3}$$

By using center wavelength of 760 nm for the laser spectrum in the PL-LS-SD-OCT system, and $d = \frac{1000\mu m}{1200}$, we get $\alpha = 25.6$ degrees.

In the detector arm simulations, point light sources were used to mimic the signals scattered from the sample. Three fields, each containing three wavelengths, 660 nm, 760 nm, and 860 nm, are placed along the center vertical line with a separation of 0.3 mm to represent the center and boundaries of 80% of the sample illumination from section 3.2.1.

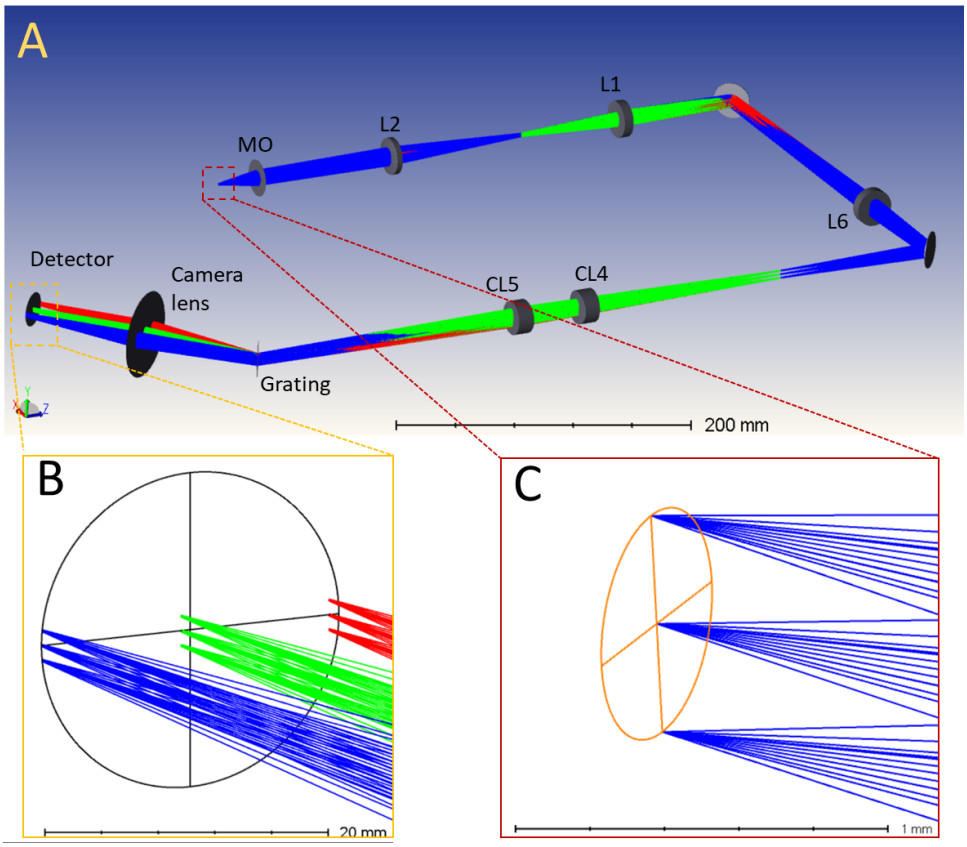

Figure 4.10 (A) 3D layouts of the detector arm. The blue, green and red colors represent the 660 nm, 760nm, and 860nm wavelength, respectively. (B) Zoomed in view of the light distribution on the detector. (C) Zoomed in view of the field setup at the sample plane.

Figure 4.10 (B) shows the location each wavelength of the field drops onto the detector. From the simulation, the distance between 620 nm and 820 nm on the detector is 21.253 mm. Given that the physical horizontal length of the detector is 19.96 mm, the mismatch between the projected line and the width of the sensor will cause ~5% loss the spectral information, which will proportionally shorten the scanning range of the PL-LS-SD-OCT system. Since originally the system was designed to have a scanning range of 1.8 mm while the typical human cornea thickness is ~ 600 μm (corresponding to optical thickness of ~ 830 μm assuming average refractive index of the corneal tissue of 1.38), the 5% shortening of the system's scanning range will not affect significantly its ability to image the human cornea. In the spatial direction, the OCT signal projected onto the camera sensor has a physical length of 6.05 mm which corresponds to 775 pixels.

4.2.4 Spectrometer calibration

In any SD-OCT system, the depth information is extracted by converting the wave number, k, to physical distance, d, through Fourier transformation. However, as the grating disperses the interference signal onto the camera evenly in physical space (camera pixels have identical width), the spectrum might not be distributed evenly in k-space. Therefore, to obtain correct depth data, it is necessary to assign the wavelengths on the pixels properly before the transformation. To do so, we can manually add a modulation with known characteristics to the spectrum. We block the sample arm and replace M3, the mirror at the end of the reference arm, with a microscope cover glass. The only returning signals are the reflections from the two surfaces of the cover glass, plus their interferences. Thus, the interference fringe of this setup can be written as:

$$I(k,z) = I_1 + I_2 + \phi(k,z) \qquad \text{Eq 3.4}$$

$$\phi(k,z) = 2\sqrt{I_1 I_2}\cos(2kz) \qquad \text{Eq 3.5}$$

where I_1 and I_2 are the reflected signal from the two surfaces, and phi is the phase term that is dependent on k and the optical path delay, z, between the two signals. z is a fixed value as the cover glass has a uniform thickness and refractive index. Assuming the glass is thin enough not to cause any severe aberrations and the refractive index is not wavelength-dependent within the observable range, the phase term becomes a function of k sorely.

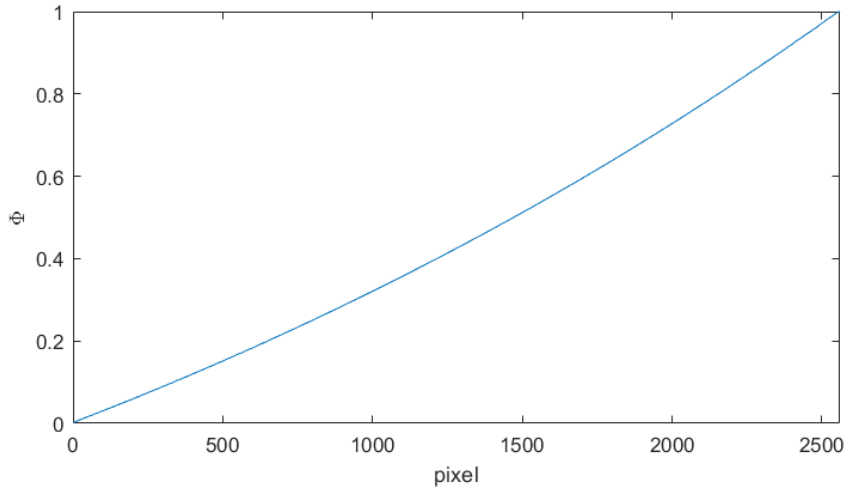

Figure 4.11 Fitted phase curve as a function of pixels

A phase curve as a function of pixels, $\phi(p)$, as shown in figure 4.11, is acquired by fitting the original phase curve onto a polynomial function. This function serves as a reference for future imaging with the same spectrometer setting. And the wavenumber is linear proportional to the curve:

$$k = a\phi(p) + b \qquad \text{Eq 3.6}$$

Though, this interpolation allows us to assign the wave numbers to the proper pixels and perform the FFT correctly, it is not enough to tell the full spectrum wavelength layout as the slope, *a*, and the offset, *b*, remains unknown. In order to locate correct wavelength of the spectrum, we placed several narrow band filters with known center transmission wavelengths. The spectra are calibrated with the phase curve $\phi(p)$, and a Gaussian function is fitted to each spectrum to identify the center peak location. Figure 4.12 shows the Gaussian fitted spectra from five bandpass filters with wavelengths of 800 nm, 780 nm, 760, nm, 740nm, and 720nmm over the calibrated linear-to-k axis. A linear function is fitted to the wavelength vs. locations data, and we can find that the maximum measurable wavelength range is from 830 nm to 610 nm.

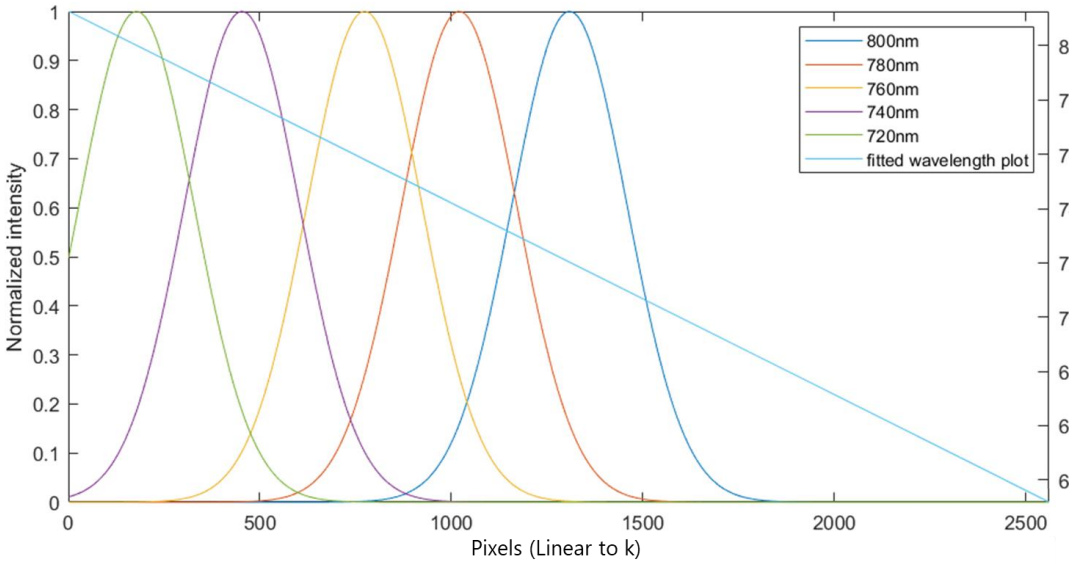

Figure 4.12 Calibrated, Gaussian fitted and normalized spectra of narrow band filters with different wavelengths and the fitted wavelength vs. linear-to-k pixel locations.

4.2.5 Maximum permissible exposure

One key feature of OCT technology in medical applications is its non-invasiveness, which is particularly important for in-vivo clinical imaging. High-power broadband light sources are used in

OCT systems to generate high axal resolution. Though higher power can increase signal strength, it also increases the risk of causing severe and irreversible damage to healthy tissues. As most ocular tissues are light-sensitive and non-regenerative, it is imperative to carefully control the incident power in ophthalmic applications. Radiation-induced ocular damage comes in two forms: thermal and photochemical damage. Thermal damage refers to a rise in temperature in the local region, which can show effect immediately with less than 10s exposure. Photochemical damage is cells malfunctioning due to overcharged molecules, which occurs with a postponed period after a longer exposure time [79].

Though the system is not designed for retinal imaging, light is still highly possible to reach the retina, thus, retinal safety should also be considered. The retina and the anterior segment of the eye, including the cornea, and the crystalline lens, are most sensitive to ultraviolet radiation below 400 nm for photochemical damage [80]. However, the spectral rage used for this project is 620 nm – 900 nm, which is outside the ultraviolet band. Besides, the system's maximum exposure time per B-scan capture is set at 2000 micro-seconds. Typically, a complete set of images for post-3D construction contains 500 B-scans, which requires one second to acquire at the maximum camera exposure time. For special imaging sessions, i.e., multiple B-scans at one location, the total imaging time usually only increases by five to six times. Even including the delay in sending the command at the start and the end of acquisition, this total imaging time will not be longer than 10 seconds. And there is usually a more than 30s gap between two 10s acquisitions. Therefore, we will estimate the maximum permissible exposure time under the <10s, >400 nm thermal damage regime.

The American National Standards Institute (ANSI 2016) provides detailed guidelines for regulating the maximum permissible exposure (MPE) in ocular imaging [81]. Related derivation and calculation for special imaging scenarios can also be found in multiple works of literature [82,83,84]. For the anterior segment of the eye and the retina respectively, the MPE irradiances for under 10 seconds of exposure within the visible and near-infrared range are:

$$E_{AS} = \sum_{\lambda=400nm}^{1400nm} E_{\mathrm{AS},\lambda} \times \Delta\lambda = 25t^{-0.75} \ [W/cm^2] \qquad \text{Eq 3.7}$$

$$E_R = \sum_{\lambda=400nm}^{1400nm} E_{R,\lambda} \times \mathrm{R}(\lambda) \times \Delta\lambda = 6t^{-0.25} \ [W/cm^2] \qquad \text{Eq 3.8}$$

where $E_{\mathrm{AS},\lambda}$ and $E_{R,\lambda}$ are the anterior segment's and the retinal spectral irradiance, $\Delta\lambda$ is the wavelength represents the summation through the wavelength interval, and $\mathrm{R}(\lambda)$ is a weighting factor that arises from ocular absorption before the retina and retinal wavelength-dependent sensitivity.

According to the simulation from section 3.2.1, the beam focuses onto the cornea with diameter of 3.826 μm in the x-direction and projects along a width of 0.6500 mm in the y-direction. The scanner provides a scanning range of ~0.3mm which is much larger than the x-direction beam width. Thus, the illumination area on the cornea is estimated as 0.3mm × 0.65mm. We can also estimate the beam dimensions on the retina assuming simple lens geometry with a focal length of 17mm for the eye; the beam that reaches the retina is 4.25 mm long in x-direction and 0.25 μm wide in y-direction, the x-direction length dominates the scanner mapping width on the retina. The beam profile produced by a Powell lens is uniform in one direction and Gaussian in the other direction. We can assume a rectangular area for simple MPE calculations. Using the given dimensions and 10 seconds as the maximum exposure time, we MPE incident power on the cornea (AS) and retina (R) are:

$$MP\Phi_{AS} = 6.93\,mW$$

$MP\Phi_R = 3.58mW$Since the beam projected on the retina is much more elongated, a more careful calculation can be performed for exposure on this rectangular area. For rectangular or slit-like beam, the energy in the elongated direction is harder to dissipate. Unlike the cornea, the retina sit at the very bottom of the eye and is surrounded by liquid and tissues, over energy deposition can cause more easily here than in the cornea. Thus, this variant calculation is more important for the retinal MPE.The equation for this special case is given as [82]:

$$MP\Phi_R = 6.93 \times 10^{-4}\, C_T\, C_E P^{-1}\, t^{-0.25} [W/cm^2] \qquad \text{Eq 3.9}$$

where parameter C_T is a function of wavelength, C_E is a function of visual angles of the illumination area, and P is the pupil factor which is a function of wavelength and exposure time. $C_T|_{\lambda<700-1050\,nm} = 1$, $C_T|_{\lambda=700-1050\,nm} = 10^{0.002(\lambda-700)}$, $C_E = 40.7$ for the current rectangular area, and $P|_{\lambda=600-700\,nm,t>0.07s} = 10^{0.0074(700-\lambda)}$, $P_{\lambda>700\,nm,t>0.07s} = 1$. Therefore, the MPE power on the retina is:

$$MP\Phi_R = 2.98\,mW$$

The current design of the system limits the optical power at the corneal surface to 2.4 mW, which is lower than all the MPE values calculated for both the cornea and retina. It should be noted the reference literature for calculations from Eq.3.9 is based on ANSI 2000, not ANSI 2016.

Chapter 5 System Characteristics and Test Results

5.1 Vertical illumination projection

To test if the Powell lens can provide a more uniform illumination than cylindrical lenses, as shown in the simulations, an USAF 1951 resolution target was used as a test sample. The reference beam was blocked completely, allowing only reflected light from the target to reach the camera (equivalent to confocal microscopy configuration). The axial position of the resolution target was adjusted to place it in the focal plane of the microscope objective, while the lateral position was adjusted in such a way that the focused line beam was centered onto the largest reflective square or for the USAF target (active like reflective mirror in this case).

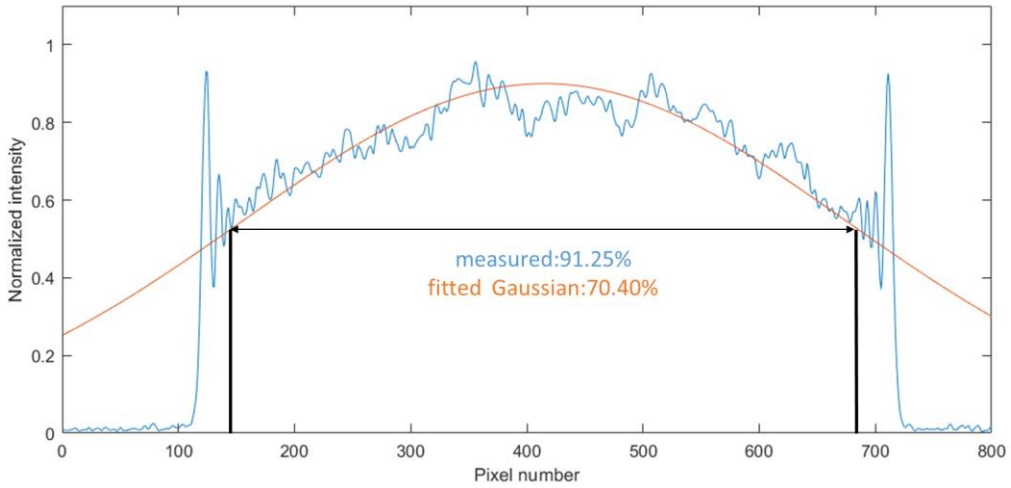

Figure 5.1 Signal profile in the vertical direction at the focal plane.

Figure 5.1 shows the profile of the beam reflected from the USAF target square and measured at the detection end of the PL-LS-SD-OCT system. Rather than having the shape shown in figure 4.8 (A), it has more similarities to figures 4.4 (B) and (E), where the beam starts to converge to the center. A Gaussian curve is fitted to the experimental data to have the same average peak and FWHM, and the area percentage under the curve between the half-power points is calculated. Though the measured Powell lens profile is not perfectly uniform, it still has about 20% more energy distributed within the center 90% range of the signal. Fine adjustment of the Powell lens position can lead to improved uniformity of the beam profile.

Figure 5.2 shows beam profiles measured away from the focal plane of the microscope objective by translating the USAF target closer to (negative direction) and farther away from the objective (positive direction). These measurements were carried out to ensure that the beam profile does not degrade too fast within a short range of the objective's focal plane. Measurements at ±100 µm and ±200 µm are shown in figure 5.2 and the beam profile remains fairly constant.

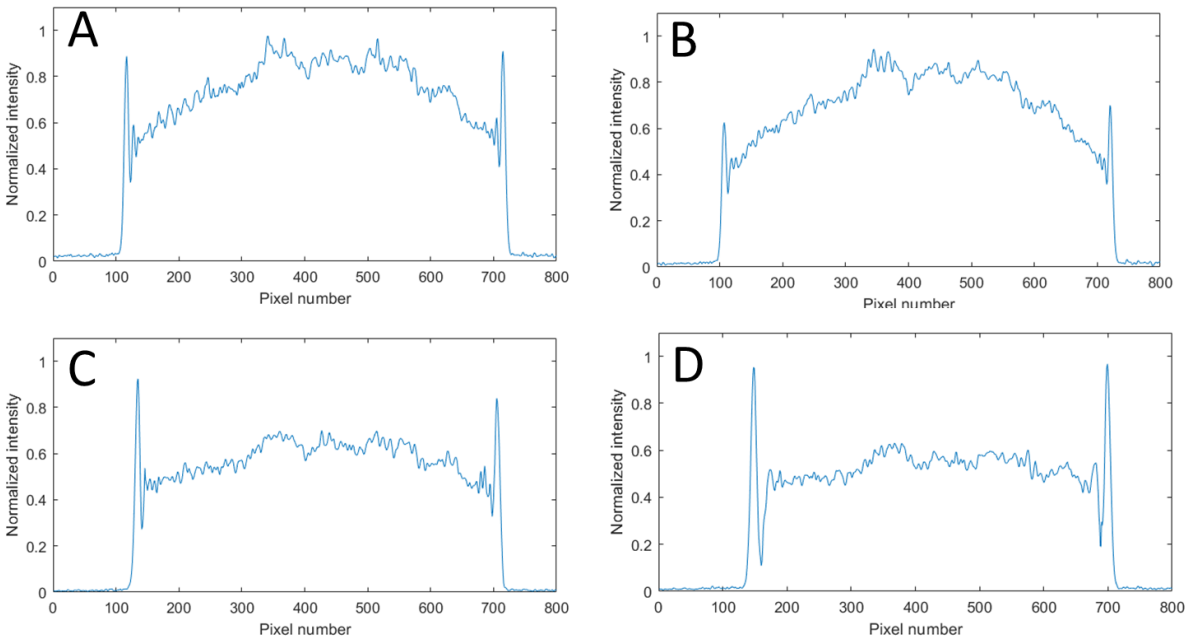

Figure 5.2 Signal profile in the vertical direction at (A) +100 µm, (B) +200 µm, (C) -100 µm, (D) -200 µm away from the focal plane.

5.2 Spectrum and axial resolution

Figure 5.3 shows the spectra measured at the detection end of the PL-LS-SD-OCT system for the reference and sample arms respectively. The sample spectrum was measured by blocking the reference beam and using a silver mirror as the test sample. The reference spectrum was measured similarly by blocking the sample beam. Note that the line beam projected onto the camera sensor illuminated 2560 pixels in the horizontal direction (spectral direction). The recorded spectra were wavelength-calibrated using the method described in section 3.2.4. As illustrated in figure 5.2, the two spectra have almost identical shapes, are centered at 720 nm and have a spectral bandwidth of 120 nm. By substituting these values into equation 2.12, we calculate a theoretical axial resolution of 1.9 µm. The plot of this

theoretical value can be obtained by applying a fast Fourier transformation (FFT) to the multiplicand of the reference and sample spectra with a cosine term.

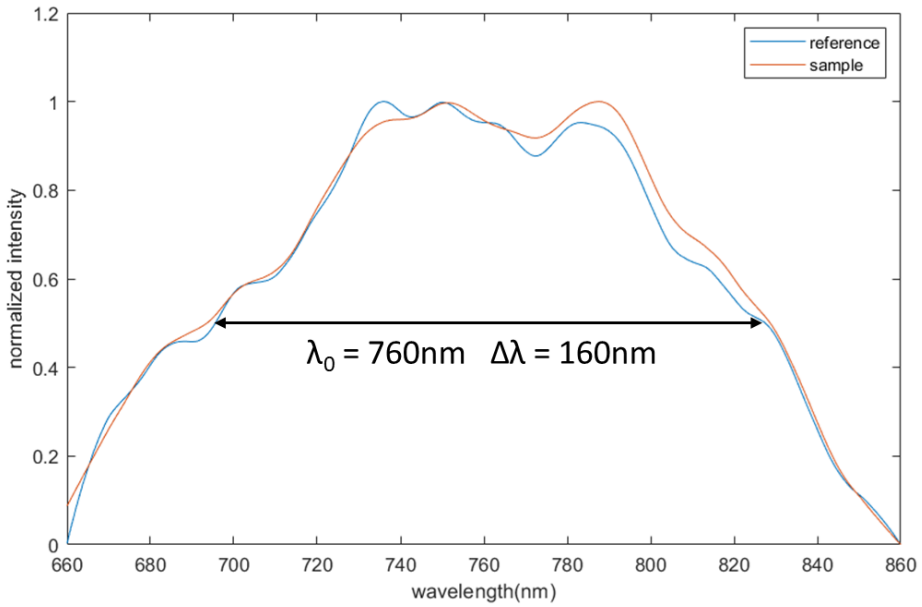

Figure 5.3 Calibrated reference and sample spectra at the center 2560 horizontal pixels.

Experimentally, axial PSF was measured by applying an FFT to the measured interference signal produced by a silver mirror used as the imaged target. As the two arms of the interferometer are comprised of different optical elements, a proper dispersion compensation (DC) is required to optimize the PSF shape and magnitude. To do so, the thickness of the prisms in the DC unit was adjusted (hardware DC compensation), then a numerical compensation up to the 5th order (software) was applied until the PSF became symmetric. Figure 5.3 shows plots for the theoretical, hardware, and software compensated point spread functions. The measured axial resolution is ~1.9 μm in air, corresponding to a ~1.4 μm resolution in corneal tissue assuming an average refractive index for corneal tissue of 1.38.

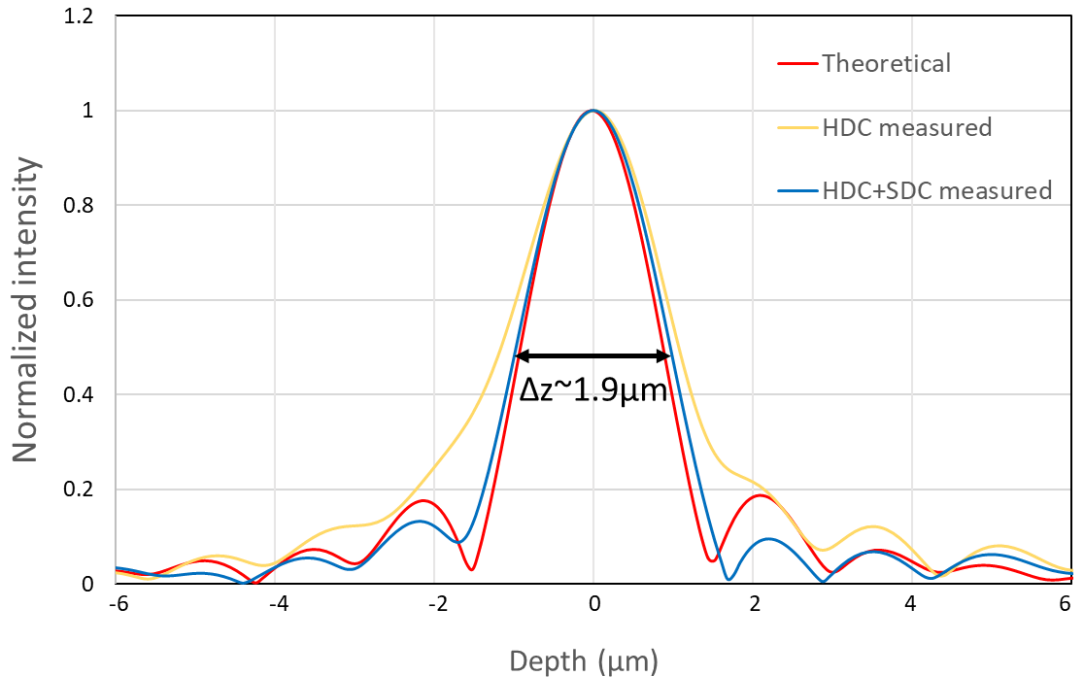

Figure 5.4 Theoretical, hardware dispersion compensated (HDC) and HDC + software dispersion compensated (SDC) axial point spread functions.

5.3 Lateral resolution

The lateral field of view (FOV) and resolutions are characterized by imaging a USAF 1951 resolution target. Figure 5.5(A) shows a sample image of the target, centered at its group five lines. The image is acquired with a 0.4 V peak-to-peak scanner voltage in the horizontal direction and is constructed with 250 x 550-pixel A-scans. The image spacing per pixel in the x and y directions can be calculated as:

$$\delta_x = \frac{l_x}{p_x}$$

$$\delta_y = \frac{l_y}{p_y}$$

where l_x and p_x the physical length and number of pixels covered horizontally in a region, while l_y and p_y are those covered in the vertical direction.

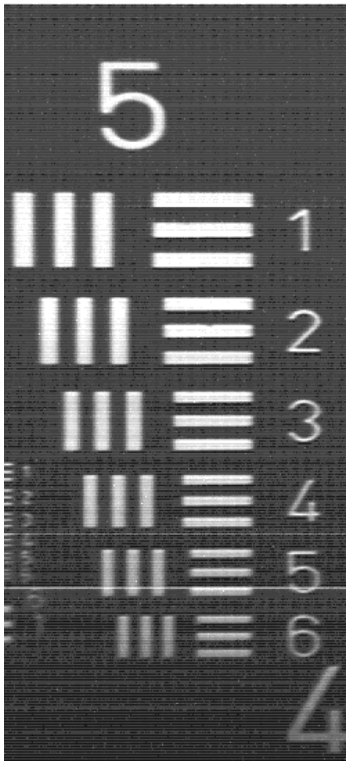

Figure 5.5 System image of group 5 of the USAF 1951 resolution target.

Group 5	Width/line (µm)	Horizontal pixels	Vertical pixels
Element 1	31.25	30	22
Element 2	27.84	27	19
Element 3	24.80	23	17
Element 4	22.10	20	15
Element 5	19.69	18	14
Element 6	17.54	15	12

Table 5.1 Width per line pair and measured pixels across a line pair from elements 1-6 in group 5.

Table 5.1 shows the average number of pixels contained in a line pair from each element of group six. Knowing the physical width of each line pair, we can then calculate the digital resolutions, $\delta_x = 1.42 \pm 0.08\ \mu m$ and $\delta_y = 1.04 \pm 0.06\ \mu m$. Thus, the total 250 x 550 pixels represents a 335 x 551 μm^2 physical FOV. It should be noted that the edges of the lines in the images are blurred due to finite system resolution. Therefore, a bright & dark pair of lines is used to estimate the digital resolution. Using only the bright or dark lines will result in over or under-estimations in the measurements. Also, a large group of elements are used as they have a high body to edge ratios, which helps reduce the measuring errors as well.

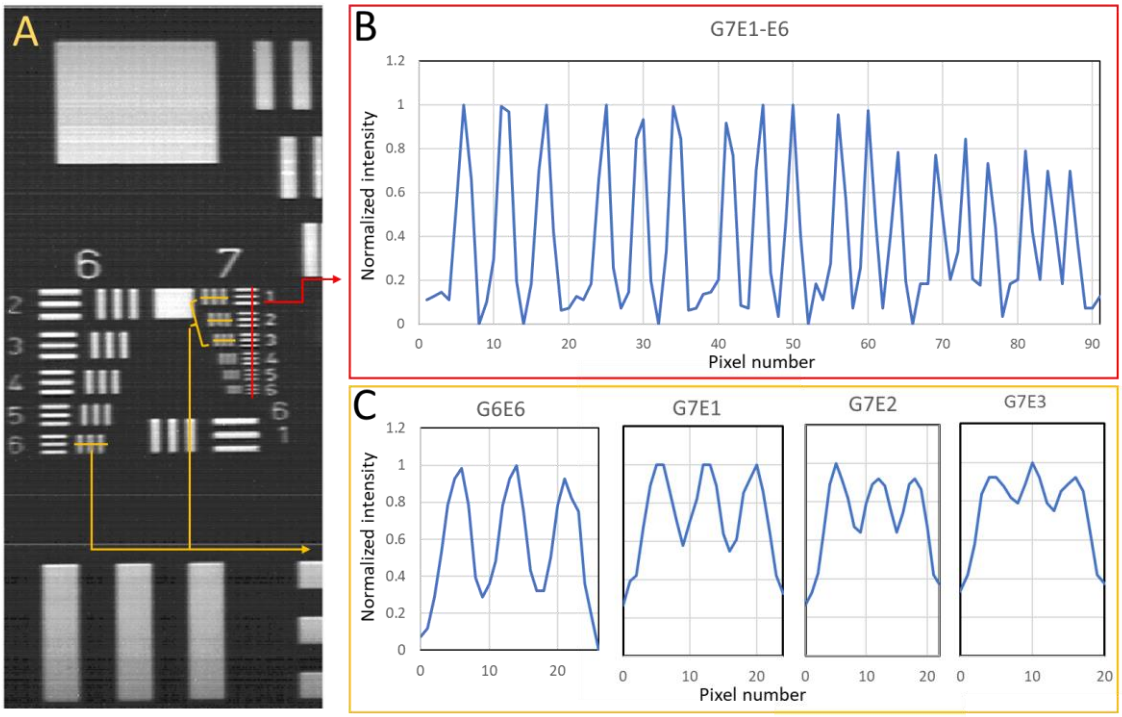

Figure 5.6 (A) System image of group 6 and 7 of the USAF 1951 resolution target. (B) Intensity profile across the horizontal bars in group 7. (C) Intensity profile across of the vertical bars from group 7 element 1, 2 and 3.

The smallest resolvable elements from the target image were used to determine the system's lateral resolution. Figure 5.6 (B) and (C) show the intensity profiles from the selected lines indicated in figure 5.6 (A). All the horizontal lines, including element six from group seven, are well distinguished, suggesting a vertical resolution under 2.19 µm. However, in the horizontal direction, the resolution degrades as it goes to smaller elements, and the lines from group seven, element three, are barely resolvable. The peaks from group seven, element one, are discernible, but their FWHM waists overlap with each other. Therefore, the horizontal resolution should be between the width of group six, element six, and group seven, element 1, which is between 4.38 µm and 3.91 µm. This value is close to the theoretical lateral resolution, 3.82 µm, from section 3.2.1. Astigmatism was excluded from the potential causes for this lateral resolution mismatch, as the presented image has the highest resolution in both directions compared to the images at other depth locations. The vertical resolution can be improved by increasing the y-direction magnification power in the detector arm. However, this will make the light project onto more vertical pixels, decreasing the SNR. The horizontal resolution can be improved by

having a larger beam NA before entering the objective lens, however this will shorten the depth of focus at the same time.

5.4 SNR and SNR roll-off

The incident power onto the image plane was measured to be 2.4mW. As shown in figure 5.1, about 88% of the total energy is distributed onto the center 550 pixels. The camera's quantum efficiency within the detectable spectral range (630 nm - 890 nm) varies from ~ 32% to ~10%, therefore for the theoretical calculation of the expected system's SNR, we take an average of 20%. and assume that the camera acquisition rate is set 1000 fps. For the center 760 nm wavelength, the diffraction efficiency of the grating is 60%, and the reflectance of the 70:30 (R:T) beamsplitter is 70%. We also assume a 5% total power loss from all achromat doublets in the detector arm. The transmission data for the microscope objective and the camera lens is unavailable, but we can also assume a 5-10% power loss from each of them. Though, it should be noted that the microscope objective and the camera lens might produce more power loss. Then, we can calculate the theoretical SNR of 85 dB using equation 2.24

Figure 5.7 Quantum efficiency of the camera.

Experimentally, the SNR was measured by placing a silver mirror at the focal plane of the microscope objective, adding a neutral density filter of power 2 (20 dB attenuation for single pass) and adjusting the reference pathlength so that the axial PSF is located at 100 μm optical path delay away

from the zero-delay line of the system. The SNR was calculated using equation 2.24, by measuring the magnitude of the PSF and the standard variation of the noise level, then converting the calculated value from eq. 2.24 into dB and adding 40 dB (signal attenuation due to double pass of the beam through the ND2 filter). The system's SNR was measured for different optical path delays to determine the SNR roll-off along the scanning range of the system (results are presented in fig. 4.6). The SNR of the system is 82 dB at 100um optical path delay and drops by 6 dB over a range of 600 µm.

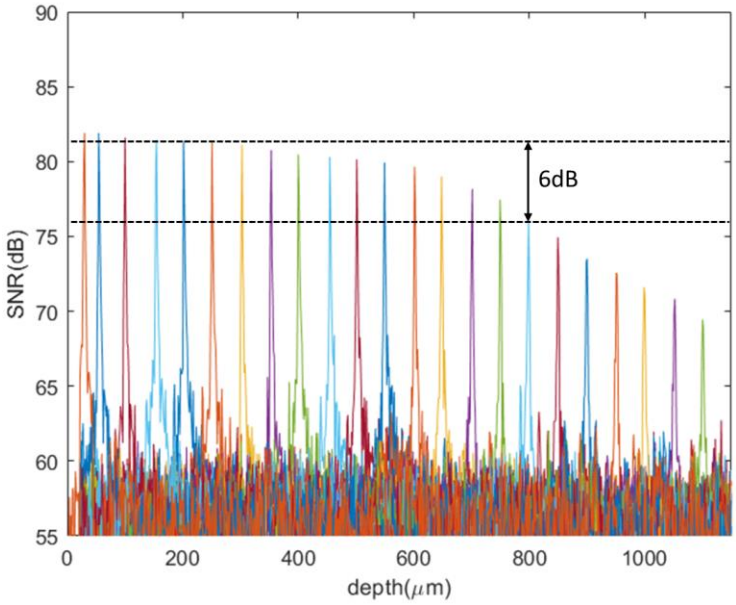

Figure 5.8 SNR roll-off from 0 to 1100 um optical path delay.

5.5 Ex-vivo images of biological tissues

5.5.1 Cucumber images

The imaging performance of the PL-LS-SD-OCT system was tested by imaging ex-vivo different biological tissues such as cucumber and mouse cornea. Due to COVID-19 related restrictions, the system was not tested for human cornea imaging. As cucumber cells have a similar water proportion and refractive index as human corneal tissues, they can serve as good sample for testing the system's performance. The images of a cucumber slice in the placental tissue and the seed region are presented in Figures 5.9 and 5.10, respectively. In the placental tissue, the boundaries of the large cells have clearly visible, and the nucleus can also be found within these large cells. In the seed region image, the

transition from large to small cells is also distinct in both y-z (B-scan) and x-z planes. A legible nucleus is identified in this image as well. Plant cell size can vary from 10 to 100 μm, and plant nucleus size are usually within the range of 1-10 μm [86]. In figure 5.10 (C), the nuclei are both about 10 μm in diameter. However, as can be seen, the right part of the image suffers from strong reflections over the top surface, causing signal loss in the area below it.

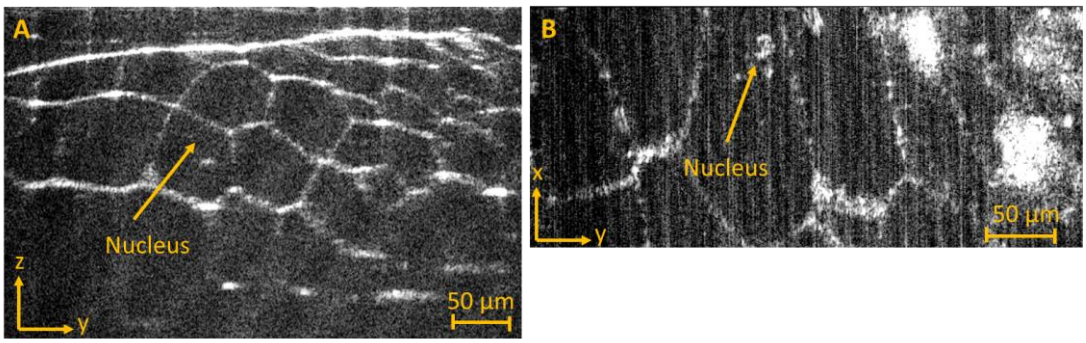

Figure 5.9. Image of the large cells in a cucumber in (A) B-scan and (B) en-face views.

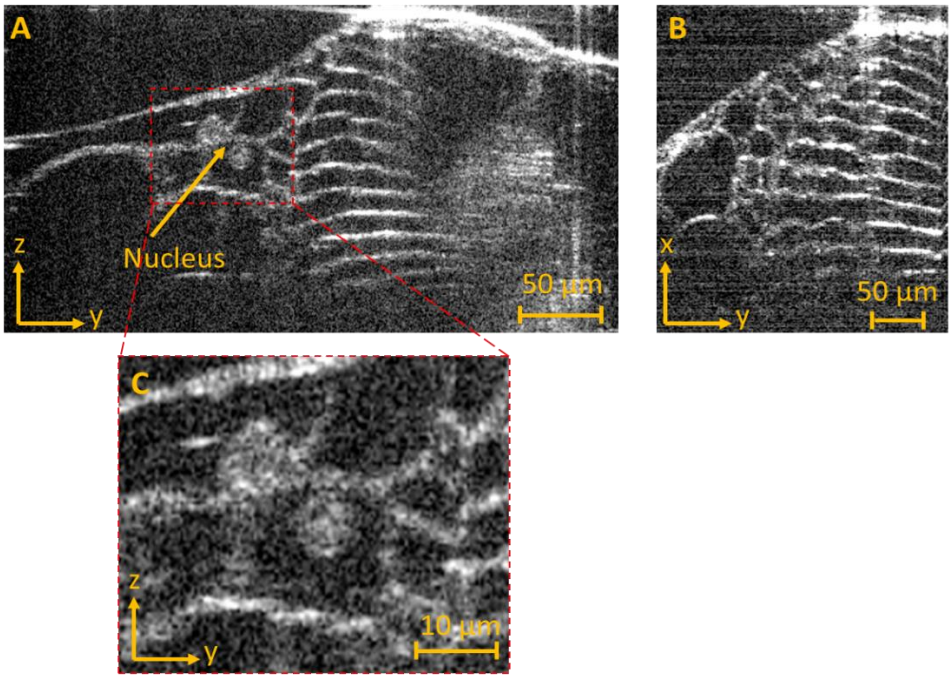

Figure 5.10. Image of a cucumber in the seed shell-endocarp transition region. (A) B-scan, (B) x-z plane slice view, and (C) zoomed-in view of the nuclei.

5.5.2 Rat cornea images

The system's performance was also tested by imaging the rat cornea. Due to COVID-19 related restrictions on live animal studies, the PL-LS-SD-OCT system was used to image the rat cornea postmortem on intact animal. Volumetric images of the corneal of a Sprague-Dawley rat were acquired within 1 hour from euthanasia. The euthanasia procedure was carried out by a certified animal technician. A selected B-scan image of the cornea is shown in figure 5.12, in which all three primary corneal layers (epithelium, stroma and endothelium), as well as stromal lamellae are visible in the image.

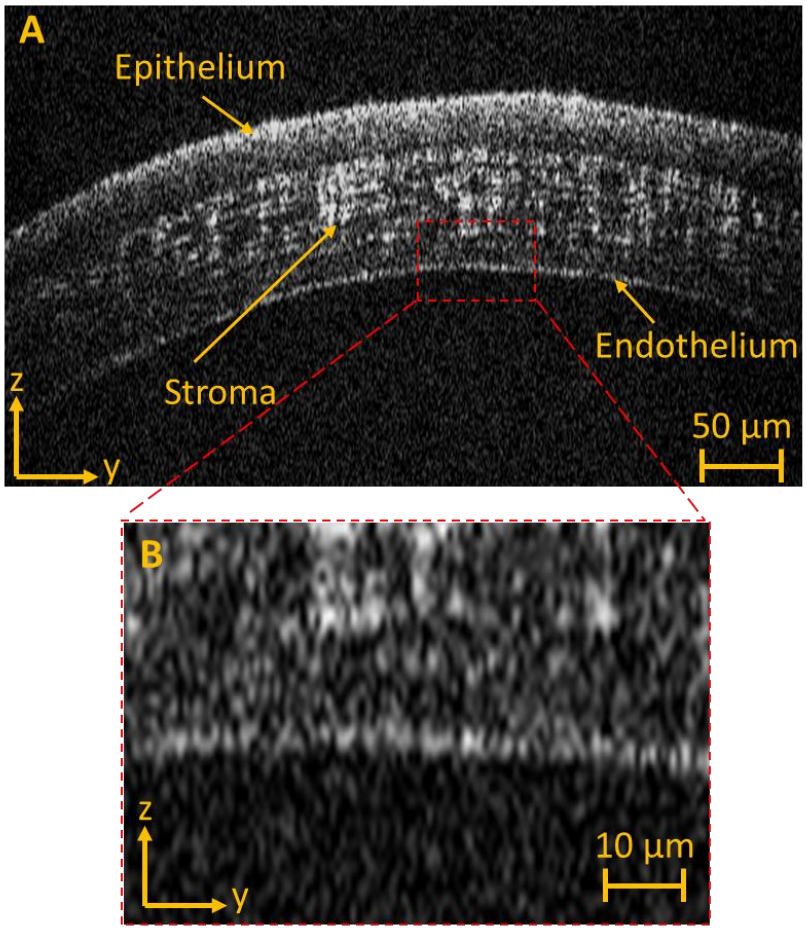

Figure 5.11. (A) Ex-vivo B-scan of rat cornea. (B) zoomed-in view of the endothelium.

The thickness of a rat cornea is about 100-150 µm which varies in different rat races [87,88], yet I was not able to find precise measurements of the cornea for the Sprague-Dawley rat from any literature

resources. The thickness of the center cornea from the image is about 130 μm. The epithelium and the stroma take about 20% and 80% of the total thickness, respectively. The zoomed-in view of the endothelial layer is shown in figure 5.11 (B), where a single cell layer structure is identified. The endothelium layer from the image is about 2-3 μm thick, which matches with the description for rat cornea from reference [87]. It should be mentioned that the Rayleigh range of the imaging beam from the simulation is only about 15 μm. For the best quality, the interface of interest should fall within this range. However, the contrast and the brightness of this image suggests that the focus lies a few dozens of microns above the endothelium, making it look dimmer. But it should also be noted that this shift of focus in the z-direction should only cause blurs to the lateral view, not the depth. The endothelium image quality can be improved through a more careful control of the focus plane position.

Chapter 6 Discussion and Conclusion

6.1 Discussion

The PL-LS-SD-OCT system design proposed in this thesis is intended primarily for cellular resolution imaging of the human cornea, therefore it was important to achieve high spatial resolution of ~2 μm or better and sustain such high axial resolution over a scanning range larger than 1 mm. The large scanning range is important as the typical optical thickness of the healthy human cornea is ~850 μm, the cornea is curved, and the OCT system's SNR degrades along the scanning range (this SNR roll-off is characteristic for all SD-OCT systems and is related to the number of illuminated camera pixels). The proposed PL-LS-SD-OCT design utilized 2560 camera pixels in the spectral direction, which corresponds to a scanning range of ~1.2 mm. The maximum SNR achieved with this design was ~82 dB for 2.4 mW optical power incident on the imaged object and for image acquisition rate of 1,000 B-scans/s.

In order to compare the performance of the proposed PL-LS-SD-OCT system with that of recently published LS-OCT systems, the systems' technical specifications are listed in table 6.1. Two of the LS-OCT systems use a cylindrical lens to generate an elliptical profile of the line beam with Gaussian power distribution along the major and minor axis of the ellipse. Therefore, those designs generate enface OCT images with progressive loss of image contrast from the center of the FOV to its periphery. Two of the published systems [12,13] use a cylindrical lens to generate the line profile of the illumination beam. Both systems used narrower bandwidth light sources that resulted in free space axial OCT resolution of 6.2 μm and 7.7 μm respectively, compared to the 1.9 μm achieved with our proposed design. Both systems achieved SNR of ~90 dB, which is ~ 8dB higher than that achieved with the proposed PL-LS-SD-OCT system. This difference can be explained with the fact that the SNR is dependent on multiple factors such as:

- **Illumination power incident on the imaged object.** The system in reference [13] used 4.4 mW incident on the corneal surface which is lower than the MPE for corneal and retinal imaging as stated in the publication. However, this value is ~2x larger than the power used in the proposed PL-LS-SD-OCT system, which accounts for ~3dB loss of SNR.
- **Detected power per pixel.** If a line beam of a certain optical power is projected onto the 3 cameras (systems from references [12] and [13] and the proposed PL-LS-SD-OCT system),

the same power will be distributed over different number of camera pixels in the spectral direction. Referring to the systems' specs in Table 6.1, it is clear that the proposed PL-LS-SD-OCT system will experience power loss of ~2x (~3dB SNR loss) compared to the system described in ref #1 and ~3x (~4.5 SNR loss) compared to the system described in ref #3. Furthermore, the detection area of each camera pixel also contributes to the system's SNR. For comparison purpose if we assume that all 3 cameras have the same quantum efficiency, then the camera used in ref#1 has square pixels of size of 14 μm, while the camera in the PL-LS-SD-OCT system has a size of 7.8 μm. The difference in the pixel's areas is ~ 4x, which is equivalent to ~6 dB difference in the measured SNR assuming that the pixels are illuminated with the same optical power.

- **Power efficiency of the optical design.** Power loss of the optical beam reflected or scattered from the imaged object along the detection arm of the OCT system will play a significant role in the system's SNR. A major difference between the optical designs reported in references 12 and 13 and the proposed PL-LS-SD-OCT system is that imaging lens. The PL-LS-SD-OCT system uses a NIR corrected microscope objective (Mitutoyo10x M PLAN APO), which has a single pass transmission loss of ~25% in the spectral range of the laser used in the system in order to achieve ~2 μm lateral resolution. The systems reported in references [12] and [13] were designed for human retina imaging and therefore use NIR antireflection coated achromat doublets that offer single pass transmission loss of <2%. This difference in transmission efficiency will account for > 10 SNR loss in the proposed PL-LS-SD-OCT.

- **Random Intensity Noise (RIN) of the light source.** The systems in references 12 and 13 used superluminescent diodes that offer much lower RIN levels compared to the NKT laser used in the PL-LS-SD-OCT system. This difference can account to ~ 3dB loss in SNR.

- **Camera acquisition rate.** There is inverse liner relationship between the camera acquisition rate and the LS-OCT systems' SNR. While the camera in the PL-LS-SD-OCT can reach frame rates > 6,000 fps for the selected sensor area (2560 ×500), the frame rate was intentionally reduced to 1,000 fps for the SNR measurements and the mouse cornea imaging, in order to compensate the SNR loses described in the paragraphs above.

	Axial resolution (µm)	Lateral resolution (µm)	Sample incident power (mW)	Pixel # in the spectral direction	Pixel size (µm)	Scanning range (mm)	Frame rate (Hz)	SNR (dB)
CL-based LS-OCT [12]	6.2	2.5	4.4	1280	20	1.98	2500	91
CL-based LS-OCT [13]	7.7	2.4	3.2	768	14	1.48	2500	90
PL-based LS-OCT [75]	2.0	6.2	15	1280	10	0.64	3500	87
Our PL-based LS-OCT	1.9	x: 4.0; y:2.1	2.4	2560	7.7	1.22	1000	82

Table 6.1 System key specs comparison from the work by Sabesan's group [12], Leitgeb 's group [13], Chen's group [75], and the work presented in this thesis.

The use of a Powell lens in an LS-OCT to improve the line beam illumination uniformity was reported recently [75]. The reported SNR was 87 dB for 15 mW optical power incident on the imaged object and camera frame rate of 3,500 fps. However, this design offers a scanning range of only 640 µm, which is not sufficient for imaging the human cornea.

The optical components in the proposed PL-LS-SD-OCT system were selected to achieve a compromise between required spatial resolution, scanning ranges and SNR that is acceptable for corneal imaging. Then high contrast of the mouse cornea images is evidence that the somewhat lower SNR may still be sufficient to generate high contrast human cornea images. COVID-19 related commercial shortage of optical components during and restricted access to the research lab the period 2020 – 2022 have played a significant role in the fact that currently the PL-LS-SD-OCT system has

sub-optimal performance. For example, the some of the lenses used in the detection arm of the system did not have the desired focal lengths. This resulted in thickness of the line beam projected onto the camera sensor that is somewhat larger than the pixel height. This leakage accounts in part for the loser SNR, as well as the anisotropy in the lateral resolution (Δx = 2 μm, Δy =4 μm). A better alignment of the system will also improve both the SNR and the spatial resolution.

6.2 Conclusion

The main goal of this thesis was to design and build a LS-OCT system that would provide the spatial resolution, scanning range, uniform SNR over the FOV and high image acquisition rate, suitable for imaging the cellular structure of the human retina. The proposed PL-LS-SD-OCT achieved many of these requirements. It provides 1.9 μm axial resolution in free space, which corresponds to ~1.4 μm in corneal tissue assuming average refractive index of 1.38, which will be sufficient to resolve even the very thin corneal layers such as the endothelium (~4 μm), Bowman's and Descemet's membranes (each ranging in thickness of 10 μm to 16 μm). Although currently the system's lateral resolution is not isotropic, it should be sufficient to resolve endothelial cell (~ 20 μm in diameter) in enface LS-OCT images. Future improvement of the system's optical design and alignment can achieve isotropic lateral resolution better than 2 μm which should be sufficient to image epithelial cells (10 – 15 μm in diameter). Based on the mouse cornea images presented in this thesis, the current design and alignment of the system could potentially generate high contrast images of the human cornea and image acquisition rate of 1,000 B-scans/s. The lower acquisition rate may not be able to suppress all involuntary eye motion-related image artefacts. Further improvement of the system's optical design and alignment may allow in-vivo imaging with frame rates closer to the maximum camera rate of 6,000 while sustaining acceptable system SNR.

6.3 Challenges and future work

The main challenges in this work originate from the unascertained understanding of Powell lens behaviors, which sequentially brings many difficulties in optimizing the system. As mentioned in Chapter 4 and shown in the ZEMAX simulations, the Powell lens does not have a clear focus as other commercially available achromatic doublet lenses. First, it makes it very hard to optimize the position of the Powell lens relative to the following optics. In practice, a perfectly parallel beam was never obtained through a Powell and a cylindrical or spherical doublet pair. In the sample arm alignment, it was straightforward to determine the positions of the four doublets first before settling the Powell lens.

However, the microscope objective had to be aligned along with the Powell lens at the same time. The difference between the measured and simulated vertical beam profiles at various depths is evidence of the Powell lens sub-optimal alignment with respect to the other optical components in the sample arm of the interferometer.

Second, it directly results in the complex design of the system. To have a clean collimated beam in the reference arm, the source beam had to be split before it enters the Powell lens. The first version of the system was built following the classic Michaelson-Morley interferometer layout but failed to obtain a clear interference pattern. The additional two beamsplitters in the current take a significant portion of the total source power, which to some extent, goes against the original intention of using a Powell lens. The complexity of the system also brings extra difficulty in aligning the reference arm with the rest of the system. Using multiple beamsplitters produces many unwanted back reflections very close to the true signals. The returning signals from the two arms must be aligned with an angle between them to allow a complete blockage of the back reflections. However, this tilt makes it almost impossible to place a slit along the beam path to serve as a confocal gate in the x-direction. This drawback showed it effects particularly during the rat cornea imaging. Missing the confocal gate, it was difficult to reduce the strong reflections from the top surface of the cornea if the cornea were oriented too perpendicular to the imaging beam. As a result, all data sets of the rat cornea ended up with having a deeper tilt in one lateral direction. However, it should be doable to successfully install the slit through a more careful alignment. Another possible solution to the system complexity issue is still using the Michaelson-Morley interferometer design but implanting another Powell lens in the reference arm. A preliminary research work has shown that it is possible to correct the Powell lens expanded beam back to collimation by using another Powell lens, forming a dual-lens pair [85]. This idea is worth further investigation. This design can potentially achieve an even better result, as not the reference beam profile would also have a more uniform shape that can further increase the SNR on the ends.

Besides the Powell lens-related modifications, improvements can also be made on other lens choices. We can increase the magnification of the spherical lens pair in the sample arm to fill a greater portion of the objective aperture, improving the x-direction resolution. The y-resolution will remain unchanged as it is only determined by the optics in the detector arm. The objective microscope, the camera lens, and the grating are all coated for NIR wavelengths. However, a big portion of the detectable range of the camera lies below 750nm. They can cause aberrations that are not shown in the simulations, not to mention that the Powell lens has no coating for any wavelength correction. The

image quality can be improved using other choices of the optical components or the camera. However, all the parts mentioned above are usually costly, and current technologies also limit their available specs.

References

1. J.P. Whitcher, M. Srinivasan and M.P. Upadhyay, "Corneal blindness: a global perspective," Bull World Health Organ 79(3), 214-221 (2001).
2. M.S. Oliva, T. Schottman and M. Gulati, "Turning the tide of corneal blindness," Indian J Ophthalmol 60(5), 423-427 (2012).
3. M.S. Sridhar, "Anatomy of cornea and ocular surface," Indian Journal of Ophthalmology 66(2), 190-194 (2018).
4. D.W. DelMonte and T. Kim, "Anatomy and physiology of the cornea," Journal of Cataract & Refractive Surgery 37(3), 588-598 (2011).
5. J. Yamanuha, "Slit lam examination," American Academy of Ophthalmology, EyeWiki, 2021. https://eyewiki.aao.org/Slit_Lamp_Examination
6. R.L. Nirderer, C.N.J. McGhee, "Clinical in vivo confocal microscopy of the human cornea in health and disease," Progress in Retinal and Eye Research 29(1), 30-58(2010).
7. N. Lagali, B.B. Peebo, J. Germundsson, U. Eden, R. Danyali, M. Rinaldo and P. Fagerholm, "Laser-scanning in vivo confocal microscopy of the cornea: imaging and analysis methods for preclinical and clinical applications," Confocal Laser Microscopy (2012).
8. B.H. Feldman, V.Y. Bunya, M.A. Woodward, E. Baghdasaryan and S. Ahmad, "Confocal microscopy," American Academy of Ophthalmology, EyeWiki, 2022.
9. W. Drexler, J. G. Fujimoto. Optical Coherence Tomography Technology and Applications. Springer, 2008.
10. A. F. Fercher, “Optical coherence tomography,” Journal of Biomedical Optics 1(2), 157-173 (1996).
11. S. R. Chinn, E. A. Swanson and J. G. Fujimoto, “Optical coherence tomography using a frequency-tunable optical source,” Opt. Lett. 22(5), 340-342 (1997).
12. V. P. Pandiyan, X. Jiang, A. Maloney-Bertelli, J. A. Kuchenbecker, U. Sharma, and R. Sabesan," High-speed adaptive optics line-scan OCT for cellular-resolution optoretinography," Biomed Opt. Express 11(9), 5274 (2020).
13. L. Ginner, A. Kumar, D. Fechtig, L.M. Wurster, M. Salas, M. Pircher and R.A. Leitgeb, "Noniterative digital aberration correction for cellular resolution retinal optical coherence tomography in vivo," Optica 4(8), 924-931 (2017).

14. U. Fares, A.M. Otri, M.A. Al-Aqaba and H.S. Dua, "Correlation of central and peripheral corneal thickness in healthy corneas," Contact Lens and Anterior Eye 35(1), 39-45 (2012).
15. N. Polisetti, N. C. Joyce, "The culture of limbal stromal cells and corneal endothelial cells," Corneal Regenerative Medicine, 131-139 (2013).
16. B.H. Jeng, "Treating the nonhealing epithelial defect," CRST Europe Sept. 25-28 (2011).
17. J.P. McCulley, B. Horowitz, Z.M. Husseini, "Topical fibronectin therapy of persistent corneal epithelial defects," Fibronectin Study Group, Trans Am Ophthalmol Soc 91, 367-386 (1993).
18. B. Wirostoko, M.J. Rafii, D.A. Sullivan, J. Morelli and J. Ding, "Novel therapy to treat corneal epithelial defects: A hypothesis with growth hormone," The Ocular Surface 13(3), 204-212 (2015).
19. S.E. Wilson, J. W. Hong, "Bowman's layer structure and function: critical or dispensable to corneal functions? A hypothesis," Cornea 19(4), 417-420 (2000).
20. A. Kobayashi, K. Sugiyama, "In vivo laser confocal microscopy findings for Bowman's layer dystrophies (Thiel-Behnke and Reis- Bucklers corneal dystrophies)," Ophthalmology 114(1), 69-75 (2007).
21. D.M. Maurice, "The transparency of the corneal stroma," Vis. Res. 10(1), 107-108 (1970).
22. C. Boote, S. Dennis, R.H. Newton, H. Puri and K.M. Meek, " Collagen fibrils appear more closely packed in the prepupillary cornea: optical and biomechanical implications," Invest Ophthalmol Vis Sci. 44(7), 2941-2948 (2003).
23. M.E. Fini, B.M. Stramer, "How the cornea heals: Corneal-specific repair mechanisms affecting surgical outcomes," Cornea 24(8), S2-S11(2015).
24. B.H. Feldman, E. Bernfeld, "Corneal stromal dystrophies," American Academy of Ophthalmology, EyeWiki,2021.
25. A.O. Eghrari, S.A. Riazuddin and J.D. Gottsch, "Overview of the cornea: structure, function, and development," Prog Mol Biol Transl Sci. 134, 7-23 (2015).
26. R.C. de Oliveira, S.E. Wilson, "Descemet's membrane development, structure, function and regeneration," Experimental Eye Research 197, 108090 (2020).
27. L.J. Jeang, C.E. Margo, E.M. Espana, "Diseases of the corneal endothelium," Exp. Eye Res. 205, 108495(2021).
28. M. He and D. Wang, Y. Jiang, "Overview of ultrasound biomicroscopy," Journal of Current Glaucoma Practice 6(1), 25-53 (2012).

29. A.S. Patel, J.D. Akkara, D.W. DelMonte, M. Morkin, A. Murchinson, J.L. Alexander, J.A. Gianconi, M. Desai and A. Sheybani, "Ultrasound biomicroscopu," American Academy of Ophthalmology, EyeWiki, 2021. https://eyewiki.aao.org/Ultrasound_Biomicroscopy
30. O. Stachs, R.F. Guthoff, S. Aumann, " In vivo confocal scanning laser microscopy," High Resolution Imaging in Microscopy and Ophthalmology: New Frontiers in Biomedical Optics. (2019).
31. R.F. Gurhoff, A. Zhivov, O. Stachs, "In vivo confocal microscopy, an inner vision of the cornea – a major review," Clinical & Experimental Opthalmology 37(1), 100-117 (2009).
32. A.G. Lee, A. Kini and B.A. Othaman, "Saccades," American Academy of Ophthalmology, EyeWiki, 2022. https://eyewiki.aao.org/Saccade#cite_note-12
33. M. Rolfs, "Microsaccades: Small steps on a long way," Vision Research 49(20), 2415-2441(2009).
34. "Microsaccades," Encyclopedia of Neuroscience, Springer, Berlin, Heidelberg; 2009.
35. S. A. Kingsley and D. E. N. Davies, “OFDR diagnostics for fibre and integrated-optic system,” Electronic Letters 21(10), 434-435 (1985).
36. K. Takada, I. Yokohama, K. Chida, and J. Noda, "New measurement system for fault location in optical waveguide devices based on an interferometric technique," Appl. Opt. 26, 1603-1606 (1987)
37. R. C. Youngquist, S. Carr, and D. E. N. Davies, "Optical coherence-domain reflectometry: a new optical evaluation technique," Opt. Lett. 12, 158-160 (1987).
38. D. Huang, E. A. Swanson, C. P. Lin, J. S. Schuman, W. G. Stinson, W. Chang, M. R. Hee, T. Flotte, K. Gregory, C. A. Puliafito and J. G. Fujimoto. “Optical Coherence Tomography,” Science 254(5035), 1178-1181 (1991).
39. J. A. Izatt, M. R. Hee, E. A. Swanson, C. P. Lin, D. Huang, J. S. Schuman, C. A. Puliafito, and J. G. Fujimoto, ‘‘Micrometer-scale resolution imaging of the anterior eye in vivo with optical coherence tomography,’’ Arch. Ophthalmol. 112, 1584–1589 (1994).
40. E. A. Swanson, J. A. Izatt, M. R. Hee, D. Huang, C. P. Lin, J. S. Shuman, C. A. Puliafito, and J. G. Fujimoto, ‘‘In vivo retinal imaging using optical coherence tomography,’’ Opt. Lett. 18, 1864–1866 (1993).

41. M. R. Hee, J. A. Izatt, E. A. Swanson, D. Huang, J. S. Schuman, C. P. Lin, C. A. Puliafito, and J. G. Fujimoto, ‘‘Optical coherence tomography of the human retina,’’ Arch. Ophthalmol. 113, 325–332 (1995).

42. C. A. Puliafito, M. R. Hee, C. P. Lin, E. Reichel, J. S. Schuman, J. S. Duker, J. A. Izatt, E. A. Swanson, and J. G. Fujimoto, ‘‘Imaging of macular diseases with optical coherence tomography,’’ Ophthalmology 102, 217–229 (1995).

43. J. S. Schuman, M. R. Hee, C. A. Puliafito, C. Wong, T. PedutKloizman, C. P. Lin, E. Hertzmark, J. A. Izatt, E. A. Swanson, and J. G. Fujimoto, ‘‘Quantification of nerve fiber layer thickness in normal and glaucomatous eyes using optical coherence tomography,’’ Arch. Ophthamol. 113, 586–596 (1995).

44. H. Gerd and W. L. Lindner, “Coherence radar” and “Spectral radar”- new tools for dermatological diagnosis, J. Biomed. Opt. 3(1), (1998).

45. M. Wojtkowski, R. Leitgeb, A. Kowalczyk, T. Bajraszewski and A. F. Fercer, “In vivo human retinal imaging by Fourier domain optical coherence tomography,” J. Biomed. Opt. 7(3), 457-463 (2002).

46. A. F. Fercher, C. Ck. Hitzenberger, G. Kamp and S.Y. El-Zaiat. “Measurement of intraocular distances by backscattering spectral interferometry,” Optics Communications 117(1-2), 43-48 (1995).

47. M. Wojtkowski, R. Leitgeb, A. Kowalczyk and A. F. Fercer, “Full range complex spectral optical coherence tomography technique in eye imaging,” Opt. Lett. 27, 1415–1417 (2002).

48. F. Lexer, C. K. Hitzenberger, A. F. Fercher, and M. Kulhavy, "Wavelength-tuning interferometry of intraocular distances," Appl. Opt. 36, 6548-6553 (1997).

49. Z. Yaqoob, J. Wu and C. Yang, “Spectral domain optical coherence tomography: a better OCT imaging stratrgy,” BioTechniques 39(6), 6-13 (2005).

50. R. Leitgeb, C. K. Hitzenberger, and A. F. Fercher, "Performance of fourier domain vs. time domain optical coherence tomography," Opt. Express 11, 889-894 (2003).

51. J. F. de Boer, B. Cense, B. H. Park, M. C. Pierce, G. J. Tearney, and B. E. Bouma, "Improved signal-to-noise ratio in spectral-domain compared with time-domain optical coherence tomography," Opt. Lett. 28, 2067-2069 (2003).

52. M. A. Choma, M. V. Sarunic, C. Yang, and J. A. Izatt, "Sensitivity advantage of swept source and Fourier domain optical coherence tomography," Opt. Express 11, 2183-2189 (2003).

53. S. Radhakrishnan, J. Goldsmith, D. Huang, V. Westphal, D. K. Dueker, A. M. Rollins, J. A. Izatt and S. D. Smith, "Comparison of Optical Coherence Tomography and Ultrasound Biomicroscopy for Detection of Narrow Anterior Chamber Angles," Arch. Ophthalmology 123(8), 1053-1059 (2005).

54. Y. Pan, H. Xie, and G. K. Fedder, "Endoscopic optical coherence tomography based on a microelectromechanical mirror," Optics Letters 26(24), 1966–1968 (2001).

55. J. Sun and H. Xie, "MEMS-Based Endoscopic Optical Coherence Tomography," International Journal of Optics 2011, 1-12 (2011).

56. J.P. Ehlers, S. K. Srivastava, D. Feiler, A. I. Noonan, A. M. Rollins and Y. K. Taom "Integrative advances for OCT-guided ophthalmic surgery and intraoperative OCT: microscope integration, surgical instrumentation, and heads-up display surgeon feedback, " Plos One 9(8), e105224-e105224 (2014).

57. P. J. L. Webster, J. X. Z. Yu, B. Y. C. Leung, L. G. Wright, K. D. Mortimer and J. M. Fraser, "Inline coherent imaging of laser micromachining," 2010 International Symposium on Optomechatronic Technologies, 1-4 (2010).

58. S. Aumann, S. Donner, J. Fisher and F. Müller, "Optical Coherence Tomography (OCT): Principle and Technical Realization," Bille, J. (eds) High Resolution Imaging in Microscopy and Ophthalmology. (2019).

59. W. Song, L. Chen, L. Han, A. R. Martinez, and K. Bizheva, "400kHz, 1 μm axial resolution SDOCT for ophthalmic applications," Ophthalmic Technologies Xxxii 3 (2022).

60. M. Münter, M. Pieper, T. Kohlfaerber, E. Bodenstorfer, M. Ahrens, C. Winter, R. Huber, P. König, G. Hüttmann, and H. Schulz-Hildebrandt, "Microscopic optical coherence tomography (mOCT) at 600 kHz for 4D volumetric imaging and dynamic contrast.," Biomed Opt Express 12(10), 6024–6039 (2021).

61. W. Wieser, B. R. Biedermann, T. Klein, C. M. Eigenwillig, and R. Huber, "Multi-Megahertz OCT: High quality 3D imaging at 20 million A-scans and 4.5 GVoxels per second," Opt. Express 18, 14685-14704 (2010)

62. T. Klein, W. Wieser, R. Andr, T. Pfeiffer, C. M. Eigenwillig and R. Huber, "Multi-MHz FDML OCT: snapshot retinal imaging at 6.7 million axial-scans per second," Proceedings of SPIE 8213(1), 82131E-82131E-6 (2012).

63. K. Lee, H. Hue, J. Y. Bae, I. J. Kim, D. U. Kim, K. Nam, G.Kim and K. S. Chang, "High speed parallel spectral-domain OCT using spectrally encoded line-field illumination," Appl. Phys. Lett. 112(4), 041102(2018).

64. A. Zuluaga and R. Richards-Kortum, "Spatially resolved spectral interferometry for determination of subsurface structure.," Optics letters 24(8), 519–21 (1999).

65. Y. Nakamura, S. Makita, M. Yamanari, M. Itoh, T. Yatagai, and Y. Yasuno, "High-speed three-dimensional human retinal imaging by line-field spectral domain optical coherence tomography," Opt. Express 15, 7103-7116 (2007).

66. B. Grajciar, Y. Lehareinger, A. F. Fercher, and R. A. Leitgeb, "High sensitivity phase mapping with parallel Fourier domain optical coherence tomography at 512 000 A-scan/s," Opt. Express 18, 21841-21850 (2010).

67. D. J. Fechtig, B. Grajciar, T. Schmoll, C. Blatter, R. M. Werkmeister, W.Drexler, and R. A. Leitgeb, "Line-field parallel swept source MHz OCT for structural and functional retinal imaging," Biomed. Opt. Express 6, 716-735 (2015).

68. D. Hillmann, H. Spahr, C. Hain, H. Sudkamp, G. Franke, C. Pfäffle, C. Winter and G. Hüttmann, 'Aberration-free volumetric high-speed imaging of *in vivo* retina,' Sci. Rep. 6, 35209 (2016).

69. T. Bonin, G. Franke, M. Hagen-Eggert, P. Koch, and G. Hüttmann, "*In vivo* Fourier-domain full-field OCT of the human retina with 1.5 million A-lines/s," Opt. Lett. 35, 3432-3434 (2010).

70. B. Považay, A. Unterhuber, B. Hermann, H. Sattmann, H. Arthaber, and W. Drexler, "Full-field time-encoded frequency-domain optical coherence tomography," Opt. Express 14, 7661-7669 (2006).

71. A. Bewsher, I. Powell, and W. Boland, "Design of single-element laser-beam shape projectors," Appl. Opt. 35, 1654-1658 (1996).

72. S. Saghfi, K, Becker, C. Hahn and D. HU, “3D-ultramicroscopy utilizing aspheric optics,” Journal of Biophotonics 7(12), 117-125 (2014).

73. V. Violeti, K, B. Patel, W. Li, C. P. Campos, S. Bharadwaj, H. S. Yu, C. Ford, M. J. Casper, R. W. Yan, W. Liang, C. Wen, K. D. Kimura, K. L. Targoff and E. M. C. Hillman, “Real-time volumetric microscopy of in vivo dynamics and large-scale samples with SCAPE 2.0,” Nature Methods, 16(10), 1054-1062(2019).

74. Z. Ma, T. Guo, T. Zhang, W. Wang, H. Chen, X. Zhang and W. Yuan, “Compact Powell-Lens-Based Low-Coherence Correlation Interrogation System for Fiber-Optic Fabry-Perot Sensors,” IEEE Photonics Journal, 11(4), 1–11 (2019).

75. Z. AI-Qazwini, Z, Ko, K. Mehta and N. Chen, “Ultrahigh-speed line-scan SD-OCT for four-dimensional in vivo imaging of small animal models,” Biomedical optics express, 9(3), 1216–1228 (2018).

76. C. K. Hitzenberger, A. Baumgartner, W. Drexler, and A. F. Fercher, “Dispersion effects in partial coherence interferometry: implications for intraocular ranging,” J. Biomed. Opt. 4, 144–151 (1999).

77. A. F. Fercher, C. K. Hitzenberger, M. Sticker, R. Zawadzki, B. Karamata, and T. Lasser, "Numerical dispersion compensation for Partial Coherence Interferometry and Optical Coherence Tomography," Opt. Express 9, 610-615 (2001).

78. M. Wojtkowski, V. J. Srinivasan, T. H. Ko, J. G. Fujimoto, A. Kowalczyk, and J. S. Duker, "Ultrahigh-resolution, high-speed, Fourier domain optical coherence tomography and methods for dispersion compensation," Opt. Express 12, 2404-2422 (2004).

79. D. van Norren, J. Vos, “Light damage to the retina: an historical approach,” Eye 30, 169-172 (2016).

80. J. A. Zuclich, “Ultraviolet-induced photochemical damage in ocular tissues,” Health Phys. 56(5), 671-682 (1989).

81. American National Standards Institute, “ANSI Z80.36-2016,” Ophthalmics – Light Harzard Protection for Ophthalmic Instruments, (2016).

82. F.C. Delori, R. H. Webb, and D. H. Sliney, "Maximum permissible exposures for ocular safety (ANSI 2000), with emphasis on ophthalmic devices," J. Opt. Soc. Am. A 24, 1250-1265 (2007)
83. D. Sliney, D. Aron-Rosa, F. DeLori, F. Fankhauser, R. Landry, M. Mainster, J. Marshall, B. Rassow, B. Stuck, S. Trokel, T. Motz West, and M. Wolffe, "Adjustment of guidelines for exposure of the eye to optical radiation from ocular instruments: statement from a task group of the International Commission on Non-Ionizing Radiation Protection (ICNIRP)," Appl. Opt. 44, 2162-2176 (2005)
84. R. Landry, R. Bostrom, S.Miller, D. Shi, D. Sliney, “Retinal phototoxicity: A review of standard methodology for evaluating retinal optical radiation harzards,” Health Physics 100(4), 417-434 (2011).
85. O. Willstrand, Intensity distribution conversion from Gaussian to Top-Hat in a single-mode fiber connector, 2013.
86. H. Smith, The Molecular Biology of Plant Cells. University of California Press, 1977.
87. S.M. Molon-Noblot and P. Duprat, "Anatomy of the ocular surfaces, cornea, and conjunctiva, rat and mouse," Eye and Ear, Springer, 1991.
88. J. T. Henriksson, A. M. McDermott, and J. P. G. Bergmanson, "Dimensions and morphology of the cornea in three strains of mice," Invest Ophthalmol Vis Sci 50(8), 3648-3654.

Appendix A
Contact Lens Study

Before starting the LS-OCT project, I participated in the contact lens using an existing point-scan SD-OCT system built by former students from the group. The project required in-vivo imaging of the patient and was paused since the pandemic due to regulations. I here present the work I contributed to this study and the preliminary results.

Introduction

The market for contact lenses keeps growing as refractive error becomes a more prevalent issue for people all over the world. However, approximately 50% of all contact lens wearers stop contact lens wear within three years of commencing wear. The primary reason for discontinuation is related to contact lens discomfort, and this figure has not changed over the past 30 years, despite significant improvements in contact lens materials, disinfection systems, and shorter replacement periods. A recent systematic review of the literature shows that one of the major determinants of contact lens comfort is the interaction between the lens edge and the peripheral cornea and conjunctiva. While the importance of this interaction is well accepted, methods to analyze it at high resolution do not exist currently in either a research or clinical setting. Studies to examine this are critical to understanding this complex interaction.

Ultrahigh resolution optical coherence tomography (UHR-OCT) offers the high spatial resolution necessary to image and characterize structural and blood flow changes in the human conjunctiva and sclera caused by the contact lens edge during wear of soft contact lenses. UHR-OCT images can provide quantitative metrics such as depression of the conjunctiva and sclera by the contact lens edge, temporary or permanent loss of conjunctival cells and scleral neovascularization of the tissue at and near the contact lens edge. Such quantitative metrics can be used to investigate contact lenses of novel design of the lens edge or novel materials. The main goal of this study is to examine such morphological and vascular changes in the conjunctiva and sclera associated with wear of different types of soft contact lenses.

Methods

The research grade UHR-OCT system used in this study combines axial resolution of ~1.5 μm in biological tissue with image acquisition rate of 250 kHz. The light source is a femtolaser with emission spectrum centered at ~790 nm and spectral bandwidth of ~135 nm. A 5x/0.14 NIR corrected microscope objective was used in the UHR-OCT imaging probe to achieve lateral resolution < 4 μm and FOV of ~3 mm × 3 mm.

Participants in this study were habitual contact lens wearers with healthy normal corneas. Contact lenses from different manufacturers, of different materials and design of the lens edge, were tested. Volumetric UHR-OCT images (1000 x 500) were acquired from 3 locations in the peripheral cornea and conjunctiva (inferior, nasal and temporal). The images were processed with custom MATLAB-based algorithm and rendered in 3D with commercial software (Amira).

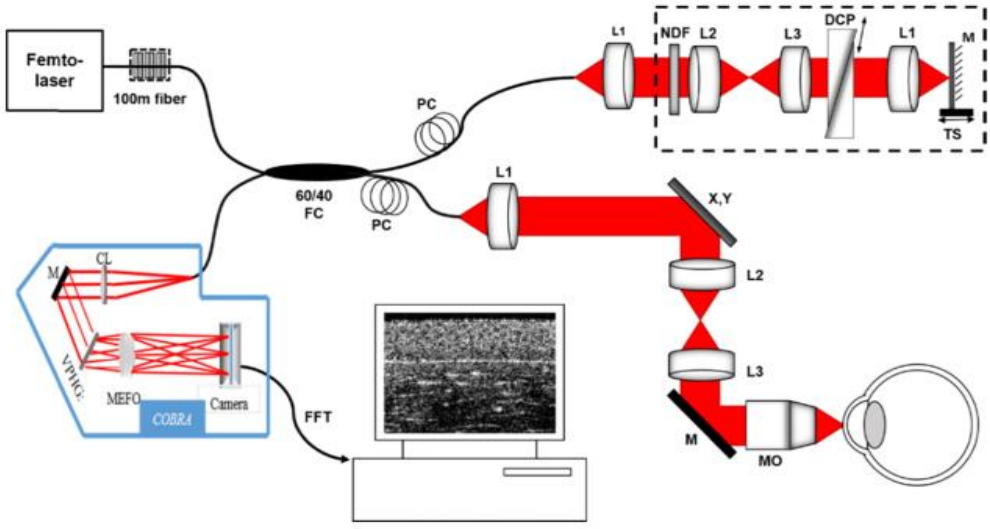

Figure Appx. 1. Schematic of the UHR-OCT system. CL – collimator; DCP – dispersion compensation prisms; FC – broadband fiber coupler; L1 to L4 – lenses; M – mirror; MO – Microscope objective; NDF – neutral density filter; PC – polarization controllers; X,Y – galvanometric scanners; VPHG – volume phase holographic grating [I].

Results and Discussion

Figure Appx.2 shows representative cross-sectional (A) and volumetric (B) OCT images of the edge of a soft contact lens and the surrounding ocular tissue at the temporal location of the eye. The indentation of the conjunctival tissue can be clearly observed in the 2D and 3D images. This indentation is caused by 2 effects: physical depression of the conjunctival tissue due to the weight of the contact lens and an optical artefact associated with the difference in refractive indices of air (n = 1), the contact lens material (n = 1.4) and biological tissue (average n = 1.38) and the fact that OCT measures optical path differences.

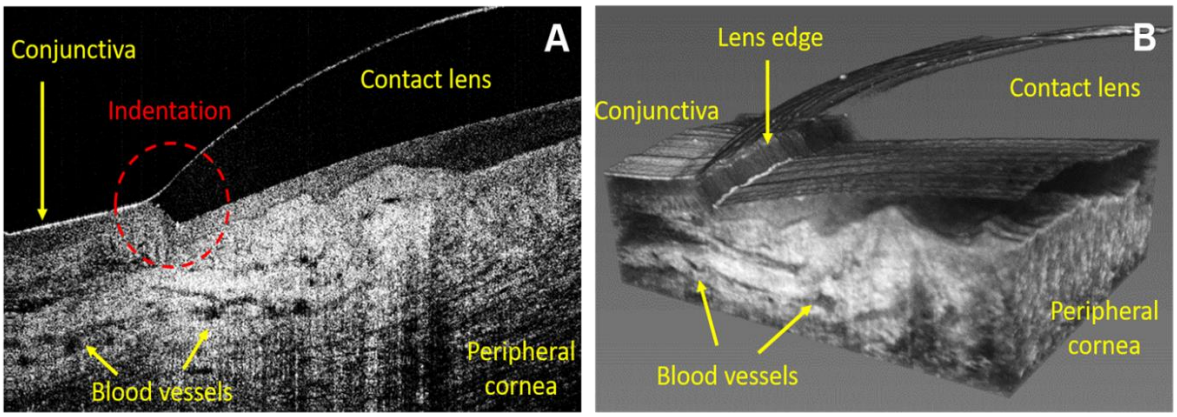

Figure Appx. 2. Cross-sectional (A) and volumetric (B) images of the contact lens edge, the peripheral cornea and conjunctiva acquired from the nasal location of the eye.

In order to correct for the refractive index difference associated image artefact, OCT images were acquired from a calibration phantom [II], consisting of a contact lens placed over the surface of a glass ball of known refractive index. A representative OCT B-scan of the calibration phantom is shown in Figure Appx. 2(A). Next, a custom Python-based algorithm was developed to automatically segment the surfaces of the contact lens and the ball and then correct for the optical artefact. Example performance of the algorithm is presented on Figure Appx. 2(C).

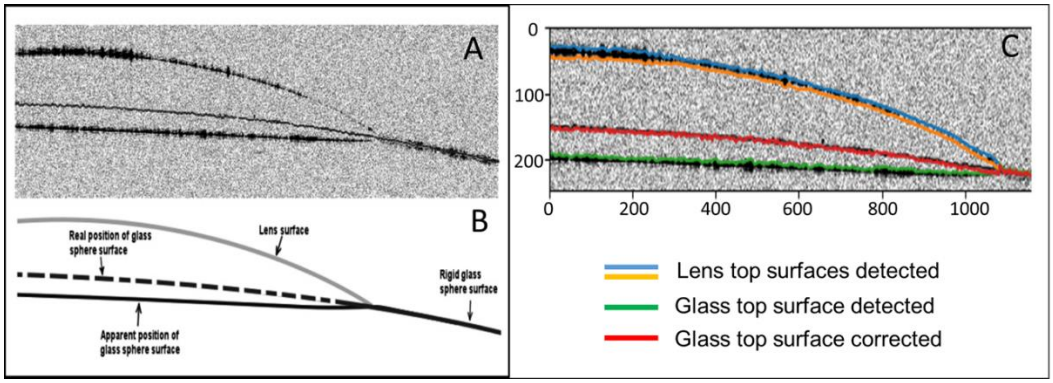

Figure Appx. 3. Cross-sectional OCT image of a soft contact lens placed on top of a glass sphere with a known refractive index (A). Schematic diagram that shows the optical artefact. Colored lines generated by the segmentation routine of the Python algorithm are overlayed with the original OCT image of the calibration phantom (C).

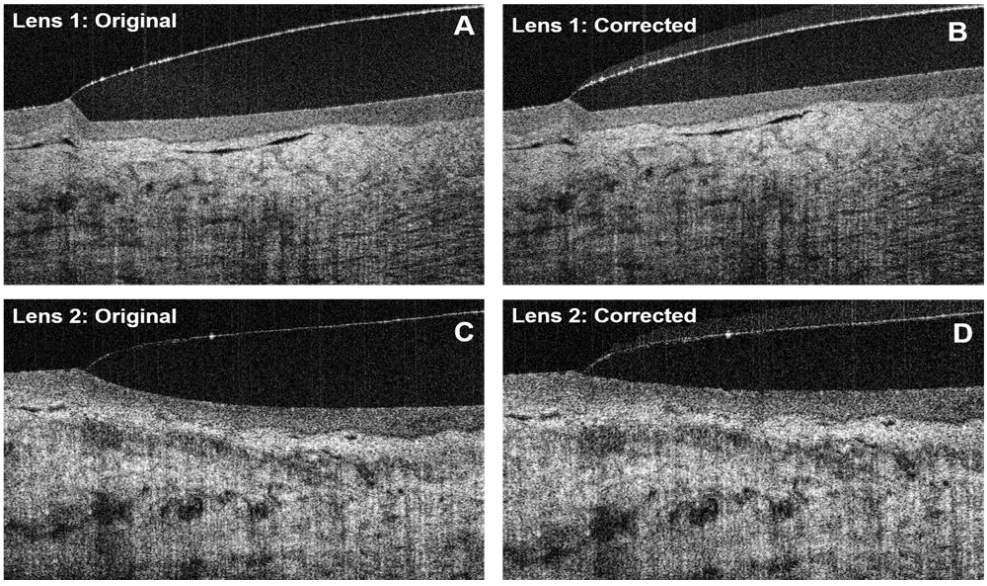

Figure Appx. 4. Original and corrected OCT images of the edges of 2 different types of contact lenses, acquired from the temporal location of the same subject.

The images in figure appx. 4 show the difference in the contact lens edge design. Lens #1 has a “sharp” edge design that causes significant depression of the conjunctiva. Lens #2 has a tapered edge design and causes a much smaller depression of the conjunctival tissue (Fig. Appx. 4(D)).

Conclusion

We used a high-speed UHR-OCT system to image the periphery of different soft contact lenses and the ocular tissue below the lens edge. We developed and tested an automatic algorithm to correct the optical artefact introduced by the refractive index of the lens material and thus to separate and quantify the mechanical deformation of the conjunctival and scleral tissue under the lens edge. Results from this study will provide valuable information on how the contact lens design and material are related to the observed tissue changes. Such feedback can aid future development of contact lens designs and edge forms.

References

I. B. Tan *et.al*., "250 kHz, 1.5 μm resolution SD-OCT for in-vivo cellular imaging of the human cornea," BOE 9, 6569-6583 (2018).

II. L. Sorbara *et al*. Optical edge effects create conjunctival indentation thickness artefacts. Ophth and Phys Optics, 35(3):283–292 (2015).